

The oxidation behavior of Mg-Er binary alloys at 500 °C

Jiajia Wu^{a,b}, Yuan Yuan^{a,b,*}, Li Yang^{a,b}, Tao Chen^{a,b}, Dajian Li^c, Liang Wu^{a,b}, Bin Jiang^{a,b}, Martin Steinbrück^c, Fusheng Pan^{a,b}

^a National Engineering Research Center for Magnesium Alloys, College of Materials Science and Engineering, Chongqing University, Chongqing 400044, China

^b State Key Laboratory of Mechanical Transmissions, College of Materials Science and Engineering, Chongqing University, Chongqing 400044, China

^c Karlsruhe Institute of Technology, Institute for Applied Materials – Applied Materials Physics (IAM-AWP), Karlsruhe 76131, Germany

ARTICLE INFO

Keywords:

Magnesium-Erbium alloys
High-temperature oxidation
Parabolic oxidation kinetics

ABSTRACT

Thermodynamics and kinetics of the oxidation behavior of magnesium-erbium (Mg-Er) alloys at 500 °C were studied. The observed protective oxidation behavior, which follows parabolic kinetics, can be attributed to the formation of compact Er₂O₃ surface layer and continuous dissolution and diffusion of Er from the matrix. The surface film of Mg-8.1Er (wt%) alloy was composed of four sublayers, with the double Er₂O₃ layers consisting of a compact fine-grain layer and an underlying coarse-columnar-grain layer providing the protective effect. A four-stage oxidation process composed of three transient reaction-controlled oxidation processes and followed by a diffusion-controlled oxides growth process is proposed.

1. Introduction

Magnesium (Mg) alloys are regarded as the next generation structural metal materials following iron alloys and aluminum alloys [1–3]. They have gained increasing interest for industrial applications, especially for aerospace, transportation, medical and 3C fields due to their low density, high specific strength and stiffness, good electromagnetic shield ability and biodegradability [4–11]. However, it is generally perceived that Mg and its alloys are easily oxidized at high temperature due to the high chemical activity of Mg and the absence of a formation of passive films. During the manufacturing at elevated temperature, such as extruding, welding, forging, and heat treatment, Mg alloys are prone to be severely oxidized or even burned [1,12,13], which seriously limits the commercial acceptance and application of Mg alloys. Therefore, improving the oxidation resistance of Mg alloys at high temperature is essential for the development of magnesium alloys meeting the needs of widespread application. The reasons of the poor oxidation resistance of Mg alloys can be summarized as the following aspects [12–18]: (i) the structure of MgO film is not compact due to its low Pilling-Bedworth ratio (P-B ratio) with value of 0.81; (ii) Mg evaporates severely at high temperatures, which raises the internal stress inside MgO film, causes the cracking of the MgO film, and accelerates the further oxidation; (iii) the exothermic oxidation generates large amount of heat and intensifies the further oxidation process and finally leads the

self-ignition.

In general, two methods, surface modification and alloying, were studied to improve the oxidation resistance of Mg alloys. Surface modification, including ion implantation and coating, can form a uniform oxide film on the surface to impede the oxidation. However, the high cost and poor self-repairing ability of surface modification also limit the method being widely applied on Mg alloys. Nowadays, many researches focused on improving the oxidation resistance of Mg alloys by alloying with reactive elements (REs), such as Ca, Be, Y, and Gd, etc. [19–27]. The REs with high affinity to oxygen exert a positive effect on improving oxidation resistance of Mg alloys, which is so-called “reactive element effect” (REE). Tan et al. [28] found that the micro-alloying of 60 ppm Be could significantly improve the high temperature oxidation resistance of AZ91, which was attributed to the reinforcement of the initially formed (Mg,Be)O oxide film on the alloy surface. You et al. [26] also showed that the oxidation of pure Mg at 500 °C can be retarded by Ca addition with the formation of a protective oxide film. In addition to these alkaline-earth elements, Rare earth (RE) elements with high oxygen affinity can also improve the high-temperature oxidation resistance of Mg alloys. Yu et al. [29,30] proved that Y plays a critical role in improving the oxidation behavior of pure Mg and Mg-Sn alloys. Wang et al. [24] studied the high-temperature oxidation behavior of Mg-Y alloys and found the increase of Y content can make the alloys exhibiting protective oxidation in 450–550 °C by forming a continuous

* Corresponding author at: National Engineering Research Center for Magnesium Alloys, College of Materials Science and Engineering, Chongqing University, Chongqing 400044, China.

E-mail address: yuanyuan17@cqu.edu.cn (Y. Yuan).

Mg-dissolving Y_2O_3 protective film. Cheng et al. [3] showed proper amount of Gd addition can enhance the oxidation resistance of AZ80–0.8Ca alloy by eliminating the low-melting β - $Mg_{17}Al_{12}$ phase to a certain extent. Shinichi et al. [31] found that adding Yb to Mg results in the formation of thermal-barrier-type Yb_2O_3 film, increasing the oxidation resistance. We also found that the oxidation resistance of Mg alloys can be improved by the addition of Gd [25]. However, most oxidation experiments of Mg alloys in literature were only conducted for a short time, commonly within several hours. The oxidation behavior of Mg alloys may change over time due to the depletion of REEs. The alloys that show protective oxidation in the early stage of oxidation process may undergo breakaway oxidation in the later stage. Therefore, it is necessary to study of the long-term oxidation behavior of alloys to accurately evaluate the service of alloys. For the long-term oxidation, the high solution REEs in the primary Mg phase are usually more promising to provide a long-term protection. In this study, Er, with around 7 at% solubility in the primary Mg phase, is selected, and the long-term oxidation behavior of Mg-Er alloys were analyzed.

The oxidation kinetics were studied based on the weight gain curves of the samples under the semi in-situ high temperature oxidation process. Morphologies and chemical compositions of the surface film were characterized using scanning electron microscopy (SEM), transmission electron microscope (TEM), X-ray diffraction (XRD) and X-ray photoelectron spectroscopy (XPS). In addition, thermodynamic calculations and diffusion calculations were performed to analyze the oxidation mechanism of the Mg-Er alloys.

2. Experimental methods

2.1. Alloy preparation

Pure Mg and commercial Mg-20 wt% Er master alloy (with 807 ppm impurity) were used as the original materials to produce the Mg-Er binary alloys. All materials were melted in steel crucibles in an electric resistance furnace, which was protected under a mixed gas of 99 vol% CO_2 -1 vol% SF_6 . Pure Mg was heated to 720 °C until it melted completely, and a certain amount of Mg-20 wt% Er master alloy was added into the melt. The melt was then isothermally held at 720 °C for 20 min for the complete dissolution of the master alloy. Then the steel crucible with melt was quenched in water. Table 1 presents the chemical compositions of pure Mg, Mg-20 wt% Er master alloy and the obtained four alloys, in which the contents of Er were determined by X-ray fluorescence spectroscopy (XRF, XRF-1800). The contents of trace impurity elements Ca, Fe, Ni, Cu was measured using a plasma-atomic emission spectrometer (ICP-AES, Optima 8000), where the trace amount of impurity Ca in obtained Mg-Er alloys comes from the impurity Ca in Mg-20 wt% Er master alloy. The ingots were cut into different blocks for the as-cast microstructure characterization and high-temperature oxidation experiment. Before the characterization and oxidation process, all samples were ground to 1200 grit SiC polishing papers and cleaned with alcohol to obtain clean and flat surface.

Table 1
Chemical compositions of the starting materials and the obtained Mg-Er alloys.

Alloy	Content of main elements			Content of impurities (ppm in weight fraction)		
	Er (wt%/at%)	Mg	Ca	Fe	Ni	Cu
Pure Mg	/	Bal.	/	35	1	10
Mg-20 wt% Er master alloy	20.2/3.6	Bal.	807	29	42	485
E1	0.5/0.07	Bal.	31	39	2	15
E2	1.9/0.3	Bal.	68	46	4	58
E3	4.8/0.7	Bal.	142	17	9	119
E4	8.1/1.3	Bal.	323	4	17	200

2.2. High-temperature oxidation procedure

The high-temperature oxidation experiments were conducted in a box furnace at 500 °C, where the ambient air was used as the oxidation atmosphere to simulate the common heat treatment of Mg alloys. The alloys were cut into 13 mm × 13 mm × 13 mm blocks for the high-temperature oxidation weight-gain test. For the long-term oxidation study, a semi in-situ analysis process was employed. During the oxidation procedure, the specimens were periodically taken out of the furnace to cool down to room temperature for weight measurement and then put back into the furnace for the continuous oxidation process. The total period of the oxidation experiment was 100 h. The weight gains during the oxidation procedure of these specimens were measured by a precision analytical balance (METTLER MS105/A) with an accuracy of 10^{-5} g. Ten measurements of weight gain at each time were taken and the mean value was selected.

2.3. Microstructural characterization

The microstructure of the as-cast and oxidized specimens were analyzed using scanning electron microscopy (FE-SEM, JEOL JSM-7800 F) equipped with energy dispersive spectroscopy (EDS), with 15 kV voltage and 12 mA current. The volume percentage of the second phase of as-cast alloys was measured via the Image-J software. The average of five images measurements of each alloy was taken for each calculation. A FEI Talos F200X transmission electron microscope (TEM) with an accelerating voltage of 200 kV was used to characterize the cross-sectional oxide film. The thin foil for TEM observation was prepared using an FEI LD Helios G5 UX focused ion beam (FIB) milling system.

X-ray diffraction (XRD, Rigaku D/MAX-1200 and D/MAX-2500PC) with Cu targets, 10–90° scanning range, 40 kV voltage, and 30 mA current was used to identify the phases of the as-cast and oxidized specimens. X-ray photoelectron spectroscopy (XPS, Thermo Scientific Escalab 250Xi) was used to analyze the valence and quantitative compositions of the surface films. The XPS data were analyzed using the Advantage software. A JX8530F Plus electron probe microanalyzer (EPMA) with 20 kV was used to obtain the concentration profile of Er with depth.

Thermodynamic calculation using the ThermalCalc software equipped with TCMG5 database was employed to calculate the binary phase diagram of Mg-Er. The FactSage (version 7.0) software package with its database was used to calculate the standard reaction Gibbs free energy of element reacted with oxygen.

3. Results

3.1. The microstructure of Mg-Er alloys

Fig. 1 demonstrates the backscattered electron images of as-cast Mg-Er alloys. The Er content detected by EDS corresponding to the zone denoted in Fig. 1 is shown in Table 2. The E1 alloy is composed of α -Mg and fine white secondary phase particles. For the E2, E3 and E4 alloys, in addition to α -Mg and secondary white phase particles, grey-white areas along the α -Mg dendrite boundaries were observed. According to Table 2, the Er contents in these grey-white areas are higher than that of α -Mg for the corresponding alloys, but far to be recognized as (Mg, Er) compounds. Therefore, these grey-white areas are supposed to be caused by the segregation of Er elements along the dendrite boundaries. These grey-white rare-earth element segregation areas were also reported by Yu et al. [32] in the as-cast Mg-Y alloys. With the increasing addition of Er, the Er contents in solid solution α -Mg and the segregated areas both increase. The volume percentages of the secondary phase particles in the as-cast E1, E2, E3 and E4 alloys are 0.06%, 0.12%, 0.11% and 0.12%, respectively, according to the calculated area-fraction of phases shown in the 2-D backscattered electron images.

With the increasing addition of Er, the general size of secondary

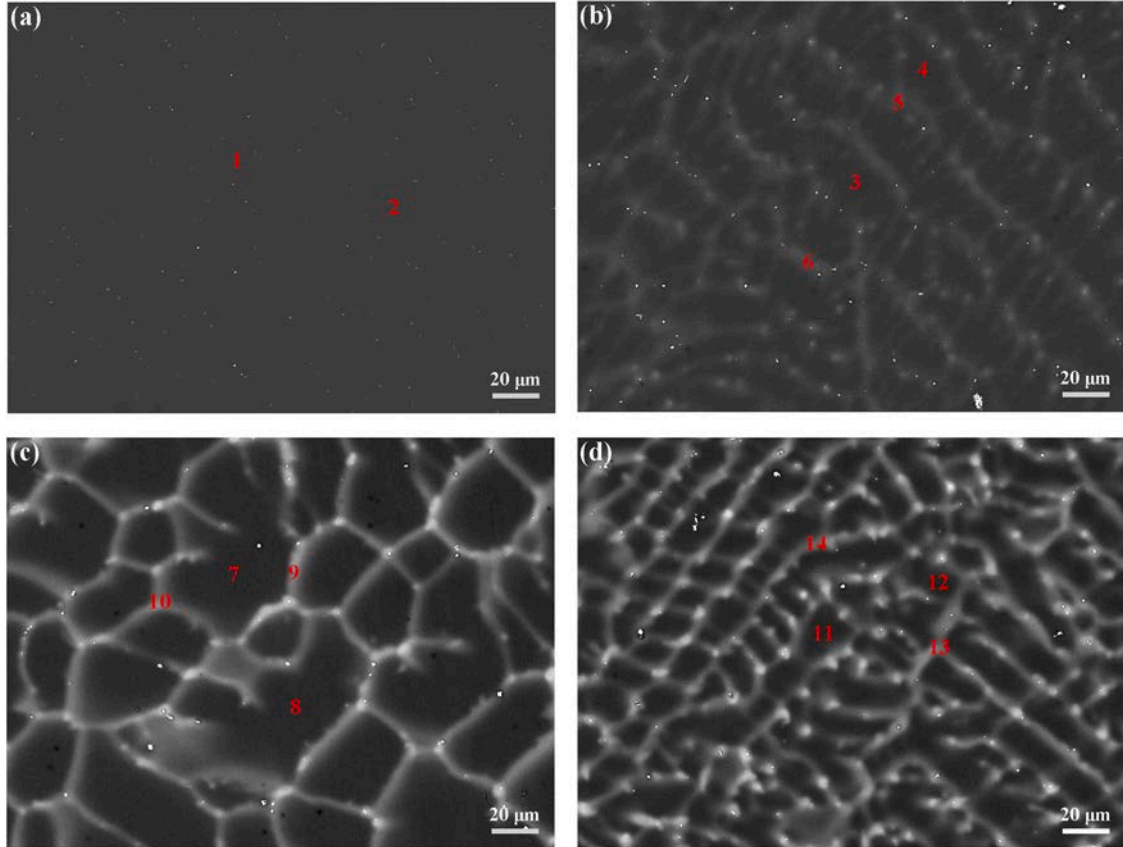


Fig. 1. The backscattered electron images of the as-cast Mg-Er alloys obtained: (a) alloy E1, (b) alloy E2, (c) alloy E3 and (d) alloy E4.

Table 2

The Er content detected by EDS corresponding to the denoted areas in Fig. 1.

Alloy	E1		E2				E3				E4			
Symbol shown in Fig. 1	1	2	3	4	5	6	7	8	9	10	11	12	13	14
Er content (wt%)	0.2	0.3	0.6	0.8	2.1	2.4	0.9	0.9	3.8	4	1.3	1.1	6.4	6.7

phase grains increases. In order to identify the white secondary phase, XRD analysis was conducted on E4 alloy and the result is shown in Fig. 2. However, it can be observed that α -Mg is the only phase presented, and the (Mg, Er) intermetallic compounds are too few to be detected by XRD.

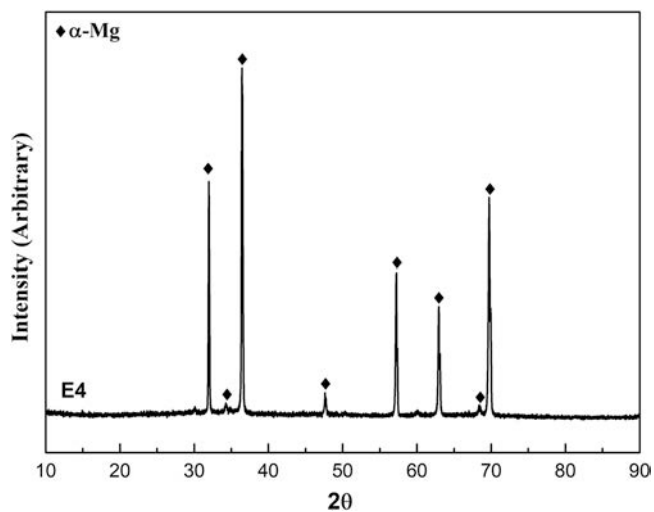


Fig. 2. XRD pattern of as-cast E4 alloy.

The entire diffraction peaks of α -Mg shift to the left about 0.2° compared with that of standard card (JCPDS#350821), which is attributed to the solid solution of Er in α -Mg, thereby causing the lattice distortion and increasing the interplanar spacing. Fig. 3 displays the binary phase diagram of Mg-Er, and it can be observed there can be four intermetallic compounds in Mg-Er alloys: $Mg_{24}Er_5$, Mg_2Er , $MgEr$ and $MgEr_2$. The EDS point analysis of the secondary phase showed that the Er content ranges from 3 to 25 wt% with the Mg content balanced. Since the sizes of these secondary phases are too small to be identified, we do not make a distinction here, and collectively mark them as the (Mg, Er) compounds.

3.2. Oxidation kinetics of Mg-Er alloys at 500 °C

Fig. 4(a) shows the weight gain curves of the Mg-Er alloys and pure Mg during oxidation at 500 °C in air, in which the weight gain test of pure Mg is conducted for comparison. As shown in the Fig. 4(a), pure Mg shows a significant weight gain compared to the Mg-Er alloys. The weight gain test of pure Mg was not continued after 22 h, because a large amount of MgO powder was formed on the surface of the pure Mg sample and fell off, leading to the inaccurate weighing. Fig. 4(b) is a regional magnification of Fig. 4(a), clearly showing the oxidation behavior of the Mg-Er alloys. In order to determine the oxidation kinetics of Mg-Er alloys, the square values of weight gain are calculated and their relation to time are shown in Fig. 4(c). It can be seen that the square values of weight gain follow a linear relationship with time

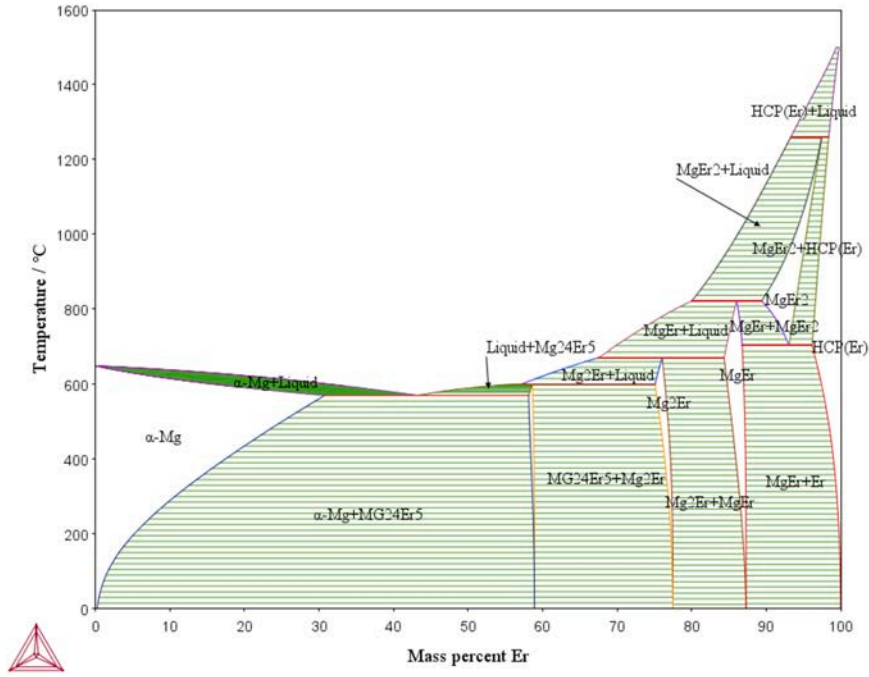


Fig. 3. The calculated phase diagram of Mg-Er system.

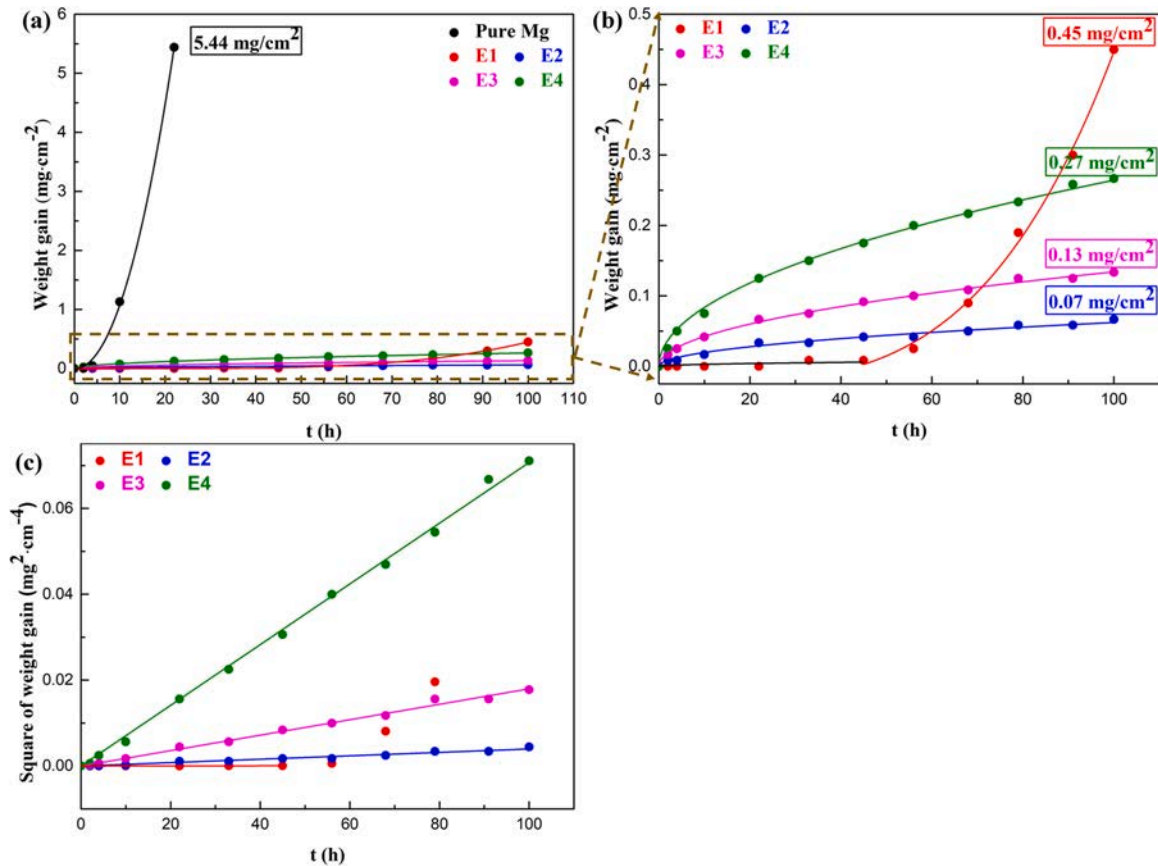


Fig. 4. Oxidation kinetic curves of pure Mg and Mg-Er alloys in air at 500 °C for 100 h: (a) weight gain curves; (b) the regional enlargement of (a); (c) square of weight gain curves.

during the whole 100 h for the E2, E3 and E4 alloys and within 45 h for the E1 alloy. When the oxidation exceeds 45 h for the E1 alloy, the weight gain curve shows an exponentially increasing, indicating the

occurrence of accelerated oxidation. The square root of weight gain can be fitted to the linear equation, which means the weight gains of alloys in an oxidation process follow parabolic kinetics. The weight gain curves

of alloys can be fitted using the following parabolic equation [33–37] and the calculated parabolic rate constants are listed in Table 3.

$$\Delta m = (k_p \cdot t)^{\frac{1}{2}} \quad (1)$$

For pure Mg shown in Fig. 4(a) and the E1 alloy oxidized beyond 45 h shown in Fig. 4(b), they show accelerated oxidation, which can be fitted to the power law using the following equation [28,35]:

$$\Delta m = A t^n + B (B > 1) \quad (2)$$

where Δm is the weight gain of the alloy per unit area (mg/cm^2), k_p is the parabolic rate constant ($\text{mg}^2 \cdot \text{cm}^{-4} \cdot \text{h}^{-1}$), A and B are fitting constants, n is the exponent, and t represents the oxidation time in hour. The fitted Eqs. (1) and (2) are displayed by the solid curves in Fig. 2(a) and (b), and the corresponding fitted parameters are summarized in Table 3.

Fig. 4(a) shows that E1 alloy exhibits two oxidation stages: (i) the initial parabolic stage; and (ii) the accelerated exponential-increased oxidation stage. However, for the E2, E3 and E4 alloys, only the parabolic oxidation kinetics were observed throughout the whole studied oxidation period. This transition of the oxidation kinetics represents the change of oxidation behavior. The parabolic oxidation is regarded as the protective oxidation, which is determined by the formation of crack-free oxide films on the surface [12,38]. On the other hand, the accelerated oxidation indicates the change of the oxidation mechanism, which is believed to be attributed to the loss of protection of oxide films [28,39].

Besides, within the parabolic oxidation stage, it is worth noting that the parabolic rate constant, k_p , increased with the content of Er, indicating smaller content of Er addition corresponds to lower weight gain values under oxidation. Similar trend was also seen in many literatures [26,29,37,40–43], such as the reports of high-temperature oxidation of Mg-Y binary alloys by Yu et al. [29] and that of Mg-Ca binary alloys by You et al. [26]. However, the reason for this phenomenon has not yet been explained in literature, and some proposed analyses are provided in Section 4.2.

It should be noted that the high-temperature oxidation test performed in this work involved cooling/heating cycles. The oxide film can crack and spall off due to the accumulated thermal/internal stress. However, as shown in Fig. 4, the weight gains of E2, E3 and E4 alloys follow parabolic law and no disturbs for the possible oxide-loss were observed during the measurement process. In addition, as later shown in Fig. 5 (in Section 3.3), the surface micromorphology of the E2, E3 and E4 alloys after oxidation is compact and undamaged. Therefore, in this work, the oxide-loss during this semi in-situ oxidation test should be negligible.

3.3. Macrographs of Mg-Er alloys after oxidation

Fig. 5 shows the macrographs of pure Mg and Mg-Er alloys after the oxidation at 500 °C for 100 h. Pure Mg was severely oxidized and a large amount of white MgO powder was formed on the surface. The MgO powder was only loosely fixed on the surface and spalled off during the handling of the sample. For the E1 alloy, a big oxide nodule can be

Table 3

Oxidation kinetics parameters fitted to the parabolic and exponential equation for pure Mg and Mg-Er alloys at 500 °C for 100 h in air.

Alloys	Time periods	Oxidation kinetics	Parameters	R ²
Pure Mg	0 < t < 22 h	Power	n 2.06, A 9.43 × 10 ⁻³	0.99
E1	0 < t < 45 h	Parabolic	k _p 7.99 × 10 ⁻⁷	0.95
	45 < t < 100 h	Power	n 3.63, A 2.54 × 10 ⁻⁸	0.99
E2	0 < t < 100 h	Parabolic	k _p 3.87 × 10 ⁻⁵	0.99
E3	0 < t < 100 h	Parabolic	k _p 1.80 × 10 ⁻⁴	0.99
E4	0 < t < 100 h	Parabolic	k _p 6.97 × 10 ⁻⁴	0.99

observed on the surface, as well as several small ones around it. The formation of oxidation nodules is regarded as the beginning of the accelerated oxidation [12]. As the oxidation progressing, oxide nodules on the surface of the alloy can quickly grow horizontally and longitudinally [38]. Here, the oxide nodules are filled with white powder (oxidation products of Mg). This loose structure cannot hinder the inward penetration of oxygen and the outward diffusion of Mg, resulting in further severe oxidation [14,15]. On the other hand, exothermic oxidation generates large amount of heat, which further intensifies the oxidation around the oxidant nodule. Hence, starting from the formation and growth of nodules, the oxidation of the E1 alloy turns into accelerated oxidation behavior. For the E2, E3 and E4 alloys, the surfaces are intact and smooth after the oxidation of 100 h, indicating oxidation-resistance property of those alloys.

3.4. The analysis of formed oxide film

The oxide films formed on the Mg-Er alloys were analyzed using XRD, XPS and SEM/EDS. Fig. 6 presents surface micrographs of the oxide films formed on the Mg-Er alloys at 500 °C for 100 h. Fig. 6(a) shows the morphology of the initial nodules and Fig. 6(b) shows the morphology of smooth area in E1 alloy. Fig. 6(c)-(h) are the morphologies of E2, E3 and E4 alloys after the oxidation at 500 °C for 100 h. In Fig. 6(a), the big nodule with a diameter of around 150 μm was surrounded with several smaller nodules with a diameter around of 10 μm. The nodules cracked and the inner white oxidation products were presented. In addition to cracks, pits caused by local oxide film shedding were also observed. Those cracks and pits act as fast transportation channels for the inward penetration of oxygen and the outward diffusion of Mg vapor, which intensifies the further oxidation [34]. For the smooth area in the E1 alloys shown in Fig. 6(b), the oxide film is intact and compact and white particles were evenly distributed on the surface. Table 4 shows the EDS composition of the denoted areas in Fig. 6. The Er contents are 25.3 wt% and 32 wt% for white particles of points 1 (E1) and 2 (E1), respectively. However, no Er is detected in the dark area of point 3 (E1) and 4 (E1). It suggests that the white particles is Er₂O₃, the dark area is MgO and the film is composed of mainly MgO with dispersed fine Er₂O₃. It is worth noting that the O contents of point 1 (E1) and 2 (E1) are larger than that of points 3 (E1) and 4 (E1), which is due to the relative high proportion of O atoms in Er₂O₃ than that of MgO.

For E2, E3 and E4 alloys, the surface films are all compact and free of crack and pit. This is associated with the protective oxidation behavior for these alloys shown by the weight gain tests presented in Section 3.2. The surface film of E2 alloy is similar to that of E3 alloy, which both are uniform and flat. However, there is loose oxide powder on the outmost surface of E2 alloy. The EDS analysis shows the atom ratio of Mg and O in points 5 (E2) and 6 (E2) are around 1:1, indicating MgO of the powder. Tan et al. [28] also reported the same loose MgO powder was formed on the oxidized Mg-60 ppm Be alloy, though the oxide film was generally compact and protective. Unlike the E2 and E3 alloys, the oxide film of the E4 alloy was covered by a large number of polygonal shaped oxide. The EDS results of points 7 (E2), 8 (E2), 9 (E3), 10 (E3), 11 (E4) and 12 (E4) shows the oxide films of the E2, E3 and E4 alloys are mainly composed of Er₂O₃.

XRD analysis was carried out to identify the formed oxides on Mg-Er alloys, the results are shown in Fig. 7. The detection of α-Mg peaks comes from the matrix, indicating thin oxide films of the alloys. For the E1 alloy, both MgO and Er₂O₃ peaks are detected. However, for the E2, E3 and E4 alloys, the major peaks come from Er₂O₃, which implies the oxides formed on the E2, E3 and E4 alloys are mainly composed of Er₂O₃. Additionally, with increasing content of Er, the peaks of Er₂O₃ intensify, indicating increasing Er₂O₃ formation.

Backscattered electron images of the cross sections and the corresponding EDS element maps for Mg, Er and O of the oxide film formed on Mg-Er alloys are shown in Fig. 8. The oxide film formed on the E1 alloy is thin and composed of discontinuous bright particles. The EDS results

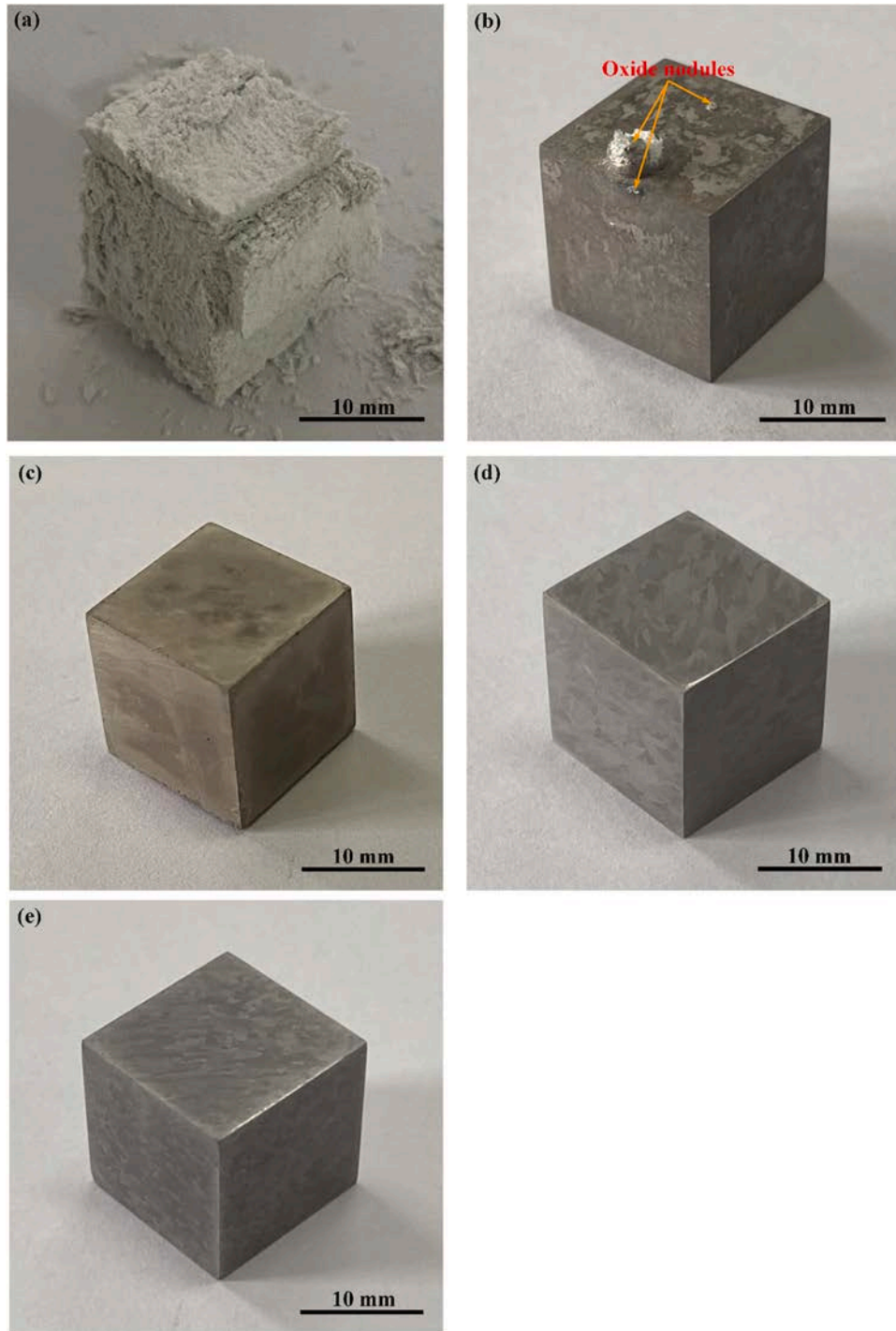


Fig. 5. Macrographs of Mg-Er alloys after the oxidation at 500 °C for 100 h: (a) E1, (b) E2, (c) E3 and (d) E4.

show the bright particles are enriched with Er, which is consistent with atomic number contrast of backscattered electron image. Therefore, it can be inferred that an intermittently distributed Er_2O_3 was formed on the E1 alloy. Unlike E1, continuous and thicker bright oxide films enriched with Er were formed on the surface of the E2, E3 and E4 alloys. The EDS analysis implies that Er_2O_3 is the main oxide product for those alloys, which is consistent with the XRD results.

Based on the above results, Er enrichment in surface oxide films of Mg-Er alloys is observed with different scales. A large amount of Er on the surface must be derived from the diffusion of Er from the matrix. In order to study the relationship between the formation of the oxide film and the matrix, low-magnification backscatter electron images of oxide

film cross sections are shown in Fig. 9. In the four alloys, white particles uniformly distribute in matrix away from the oxide film, and the particle size increases with the increment of Er content. The white particles are undissolved second phase (Mg, Er) compounds. It is worth noting that the four alloys all have a depletion zone of second phase just below the oxide film. And very few fine second phase particles were observed in the depletion zone, and their sizes are much smaller than those in the deeper matrix. The depletion of the second phase indicates the dissolution of the second phase and the release of large amounts of Er, which further diffuse to the surface to support the oxidation of the Er.

In order to further prove the existence of Er diffusion, the concentration of Er was measured with depth detected by EPMA, as shown in

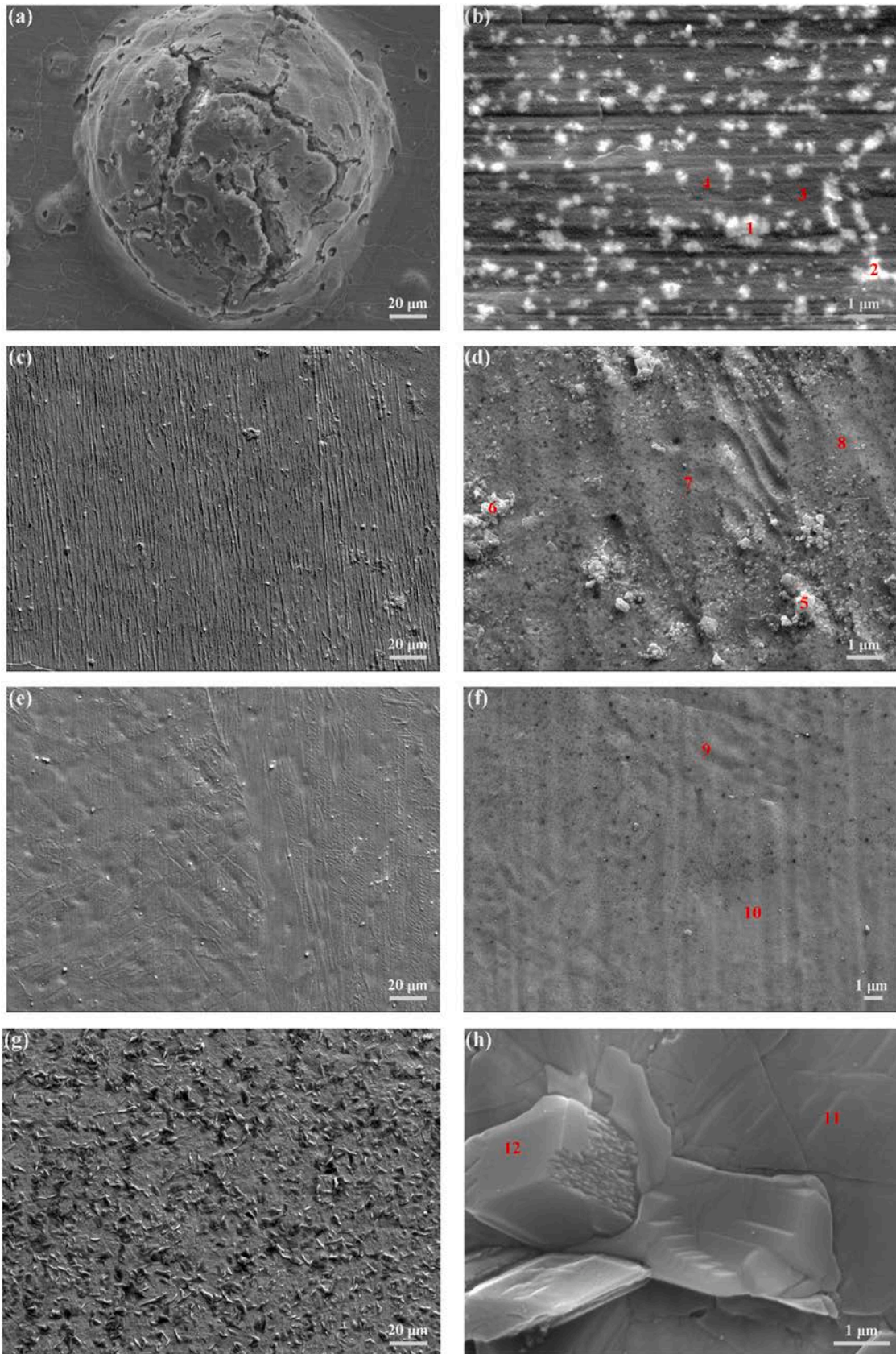


Fig. 6. Micrographs of the oxide films for the experimental Mg-Er alloys at 500 °C for 100 h in air: (a, b) E1, (c, d) E2, (e, f) E3, and (g, h) E4.

Table 4
EDS composition of the denoted areas in Fig. 6.

Alloy	Symbol	Content of element (wt%)			Content of element (at%)		
		Mg	Er	O	Mg	Er	O
E1	1	65.2	25.3	9.6	78.1	4.4	17.5
	2	59.8	32	8.2	77.7	6.1	16.2
	3	94.2	/	5.8	91.5	/	8.5
	4	95	/	5	92.6	/	7.4
E2	5	51	7.1	41.9	44.1	0.9	55
	6	56	10.4	33.6	51.6	1.4	47
	7	8.3	81	10.7	22.9	32.4	44.7
	8	9.1	79.8	11.1	24.2	30.9	44.9
E3	9	5.7	84	10.3	17	36.4	46.6
	10	4.7	85.5	9.8	14.7	38.8	46.5
E4	11	/	90.3	9.7	/	47.1	52.9
	12	/	88.6	11.4	/	42.6	57.4

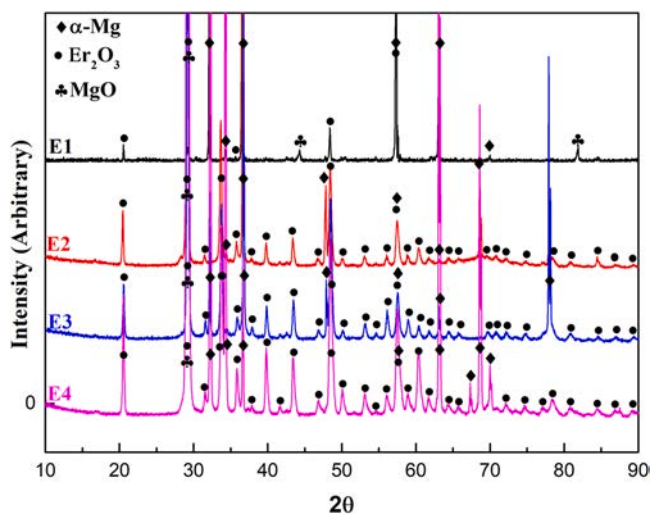


Fig. 7. XRD patterns of the oxidized Mg-Er alloys.

Fig. 10. There is Er depletion zone below the oxide film, and its concentration increases approximately linearly with the distance to the metal/oxide interface. The Er depletion zone is considered to be the Er diffusion layer, in which Er is transported from the matrix to the surface for maintaining the formation of Er_2O_3 . The thickness of the diffusion layers for the E1, E2, E3 and E4 alloys are 47 μm , 107 μm , 120 μm , and 107 μm , respectively. The Er concentration at the oxide/metal interface (abscissa is 0) cannot be directly measured by EPMA. Since the Er concentration almost has a linear relation with depth, the Er concentration at oxide / metal interface can be estimated by linear interpolation using two adjacent points. With the increasing of Er addition, the Er concentration at the oxide/metal interface also increases. As the depth increases, the content of Er is increasing linearly approximately to reach the original composition of the alloy. When the distance exceeds that of the diffusion layer, the Er contents remain stable at approximately 0.2 wt%, 1.7 wt%, 4.3 wt% and 7.4 wt% for the E1, E2, E3 and E4 alloys, respectively. These Er contents are lower than the original added Er contents, 0.5 wt%, 1.9 wt%, 4.8 wt% and 8.1 wt% for E1, E2, E3 and E4 alloys, respectively, due to the existence of (Mg,Er) compounds.

3.5. XPS analysis of the oxide film of the E1 alloy

According to the previous results obtained by XRD and SEM, the oxide film of E1 contains both MgO and Er_2O_3 . In order to quantitatively analyze the distribution of these two oxides in the oxide film of the E1 alloy, XPS analyses were performed, the results are shown in Fig. 11. Fig. 11(a), (b) and (c) are XPS depth profiling spectra of Mg 1 s, O 1 s and Er 4d regions, respectively. When the samples were followed air

exposure, the surface was covered with the adventitious carbon contamination. In order to remove the adventitious carbon contamination, pre-sputtering for 100 s before the measurement was performed. Fig. 11 (d), (e) and (f) are the XPS spectra with sputtering time 100 s of Mg 1 s, O 1 s and Er 4d regions, respectively, and Fig. 11(g), (h) and (i) are the XPS spectra with sputtering time 700 s of Mg 1 s, O 1 s and Er 4d regions, respectively. As shown in Fig. 11(d), for the sputtering time of 100 s, the Mg 1 s spectra is composed of two components. The binding energy at 1304 eV corresponds to MgO [44], and the binding energy at 1301.9 eV match to $\text{Mg}(\text{OH})_2$ [45]. However, the Mg 1 s spectra with sputtering time 700 is only contains MgO. The peaks trend in Fig. 11(a) also suggests that the mixture of MgO and $\text{Mg}(\text{OH})_2$ exists in the outmost layer of the sample. When the sputtering time increases to 200 s, $\text{Mg}(\text{OH})_2$ disappears and only MgO exists in the oxide film of E1 alloy. For O 1 s peak with sputtering time of 100 s shown in Fig. 11(e), there are two components, which are MgO with the binding energy of 529.6 eV [46] and $\text{Mg}(\text{OH})_2$ with the binding energy of 530.9 eV [45]. This agrees with the result of Mg 1 s. For the sputtering time of 700 s shown in Fig. 11(h), the O 1 s peak also contains two components, which are MgO with a binding energy of 529.6 eV [46] and Er_2O_3 with a binding energy of 531.4 eV [47]. The concentrations in atomic percent of MgO and Er_2O_3 were calculated using the software Advantage, resulting in 86% and 14%, respectively. This indicates that different oxide film depths correspond to different types of oxide films, which can be better reflected in Fig. 11(b). When the sputtering time is increased from 100 s to 200 s, the O1s peak gradually shifts to lower energy side, which is caused by the disappearance of $\text{Mg}(\text{OH})_2$. However, once the sputtering time exceeds 200 s, the O1s peak gradually shifts to the higher energy side with the increasing sputtering time, which is caused by the gradual increase of the content of Er_2O_3 from the outmost towards the inner side in the oxide film. In the case of the Er 4d spectrum, when the sputtering time is 100 s, no obvious peak appears, as shown in Fig. 11(f). However, when the sputtering time is 700 s, a peak of binding energy 168.7 eV is observed, which is associated with the presence of Er_2O_3 [48]. In the depth profile of Er 4d, as shown in Fig. 11(c), when the sputtering time is less than 300 s, no obvious peak appears. When the sputtering time exceeds 300 s, the peak corresponding to Er_2O_3 appears. Its intensity increases continuously with increasing sputtering time.

Based on the above analysis, there is a change in oxide type with the depth of the oxide film on the E1 alloy. The formed oxides on the outmost side of the oxide film are the mixture of MgO and $\text{Mg}(\text{OH})_2$. As the depth of the oxide film increases, the oxides become a mixture of MgO and Er_2O_3 , and the content of Er_2O_3 increases with the increasing depth of the oxide film. This implies that Er_2O_3 prefers to be formed on the inner side of the oxide film. Although Er_2O_3 is easy to be formed on the inner side, the largest atomic percentage of Er_2O_3 detected on the inner side of the E1 alloy is only 14%, which explains the discontinues Er_2O_3 film shown Fig. 8.

3.6. TEM analysis of the oxide film of the E4 alloy

An HAADF-STEM image and the corresponding EDS element maps for Mg, Er, Ca and O elements of the cross-sectional oxide film formed on the E4 alloy are presented in Fig. 12(a). It can be seen from the EDS element maps that the oxide film of E4 alloy is mainly composed of Er oxide. In addition, an outer layer of Ca oxide is observed, and Mg oxide is formed underneath. Since the raw material of Mg-20 wt% Er master alloy contains impurity element Ca, the E4 alloy obtained in this experiment contains 323 ppm impurity element Ca. However, since the content of Ca is small and the oxide film of E4 alloy is mainly composed of Er oxide, the influence of Ca impurity can be ignored. Fig. 12(b) presents the bright-field TEM image of the oxide film formed on the E4 alloy and Fig. 12(c)-(h) are the high-resolution images and digital diffractogram obtained by the fast Fourier transform (FFT) (inserted images). It can be seen from the bright-field TEM image that the oxide film of the E4 alloy can be divided into three regions: the outer layer of white

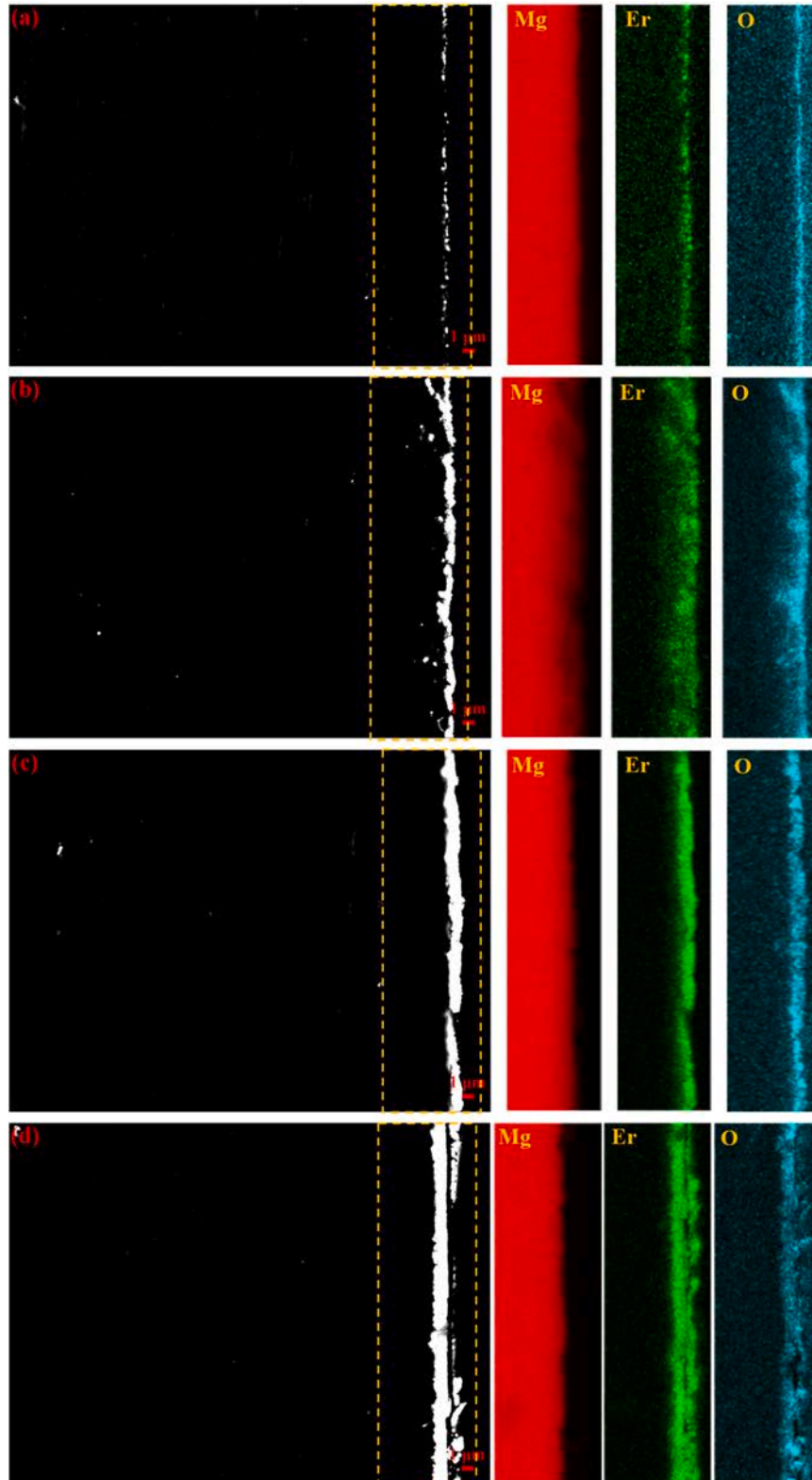


Fig. 8. BSE cross-sectional images and the corresponding EDS element maps for Mg, Er and O of the oxide film formed on (a) E1, (b) E2, (c) E3 and (d) E4.

phase A, the middle layer mixed with white phase B and dark phase C and D, and inner layer of dark phase E and F. The digital diffractogram in Fig. 12(c) shows that phase A is CaO (JCPDS #99-0070), with an fcc structure and lattice constant $a_0 = 0.481$ nm. Phase C is MgO (JCPDS #741225), with an fcc structure and lattice constant $a_0 = 0.422$ nm. Phase B, D, E and F are Er_2O_3 (JCPDS #010827), with a bcc structure

and lattice constant $a_0 = 1.054$ nm. The outer CaO layer is not uniform, and its thickness ranges from 10 to 100 nm. The thickness of the middle layer of the mixture of MgO and Er_2O_3 is about 150 nm, and it is about 800 nm for the inner homogeneous Er_2O_3 layer. It is worth noting that the Er_2O_3 formed on the inner side of the oxide film (area F) is much coarser than the outer side (area E). Shin-ichi [49] also found a similar

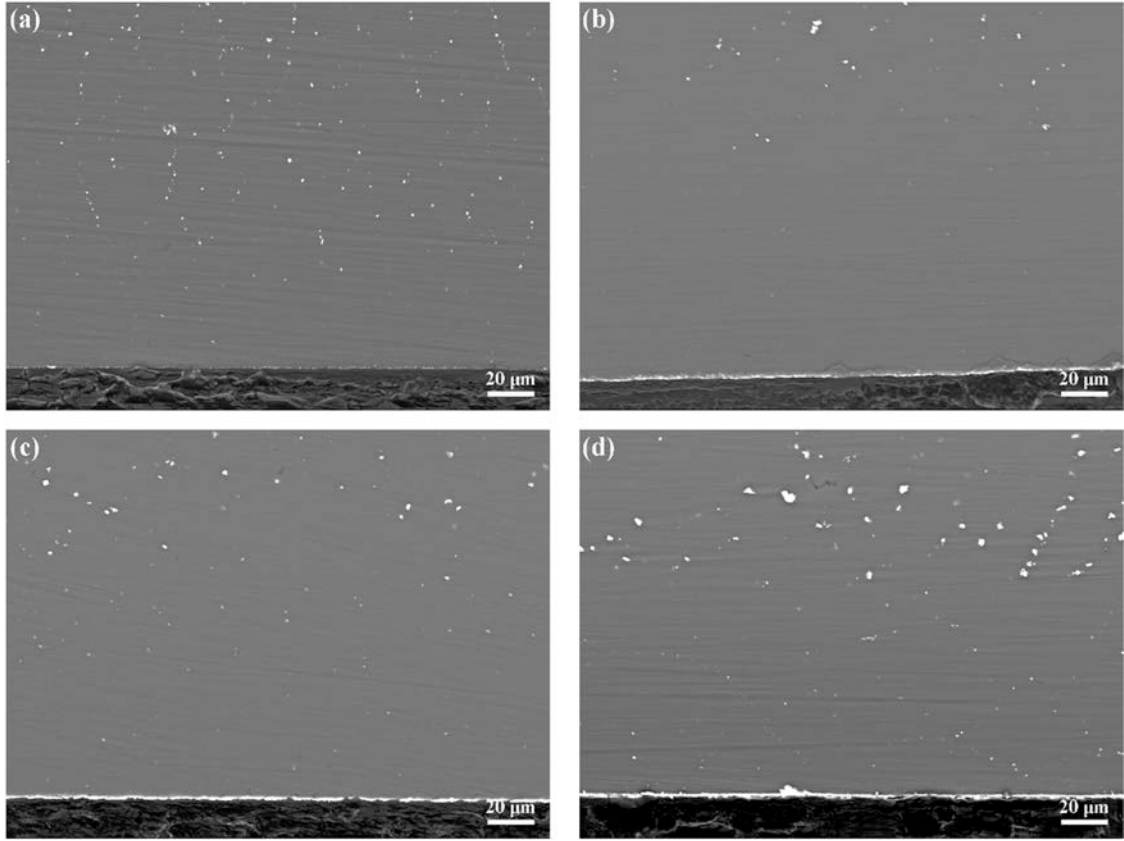


Fig. 9. Low-magnification backscatter electron images of cross-sectional oxide film on (a) E1, (b) E2, (c) E3 and (d) E4.

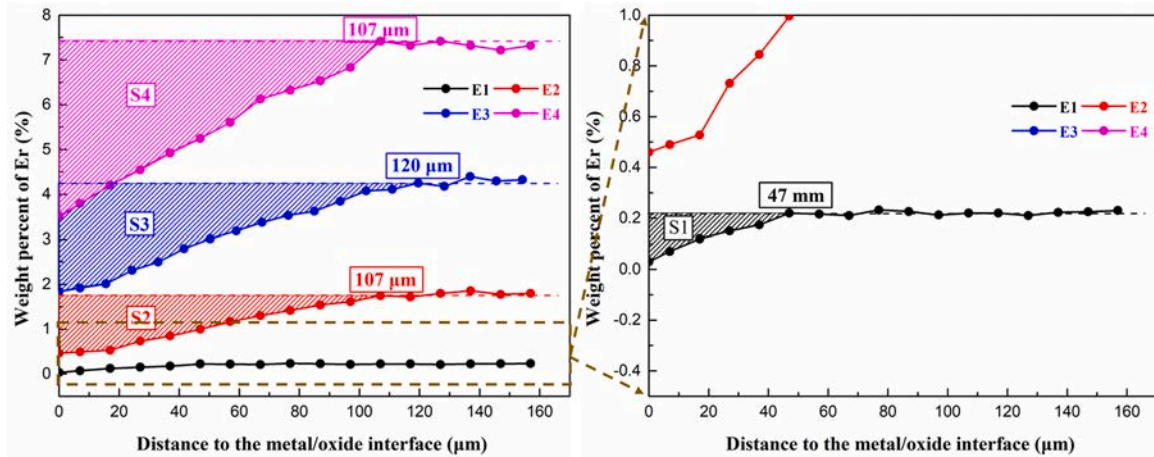


Fig. 10. The concentration of Er with depth detected by EPMA.

result that Y_2O_3 formed on the inner side is coarser than that of outer side in the oxide film of the Mg97Y2Zn1 alloy. However, the reason for the formation of such a structure has not been explained in literature.

4. Discussion

The above results show that the E1 alloy undergoes accelerated oxidation after being oxidized at 500 °C for 45 h, and a discontinuous Er_2O_3 oxide film is formed on the surface. With the Er content increases, the alloys show the protective oxidation behavior and the parabolic oxidation constants (k_p) also increases. In order to clearly understand these oxidation phenomena of Mg-Er alloys, their oxidation mechanism

is analyzed from the perspectives of thermodynamics and kinetics, including “thermodynamic analysis and oxidation process”, “the diffusion of erbium”, “comparison of oxidation kinetics of Mg-Er alloys with that of other reactive-element-containing Mg alloys” and “the oxidation stages of the Mg-Er alloy”.

4.1. Thermodynamic analysis and oxidation process

The possible chemical reactions occurring during oxidation Mg-Er alloys are as follows [50,51]:



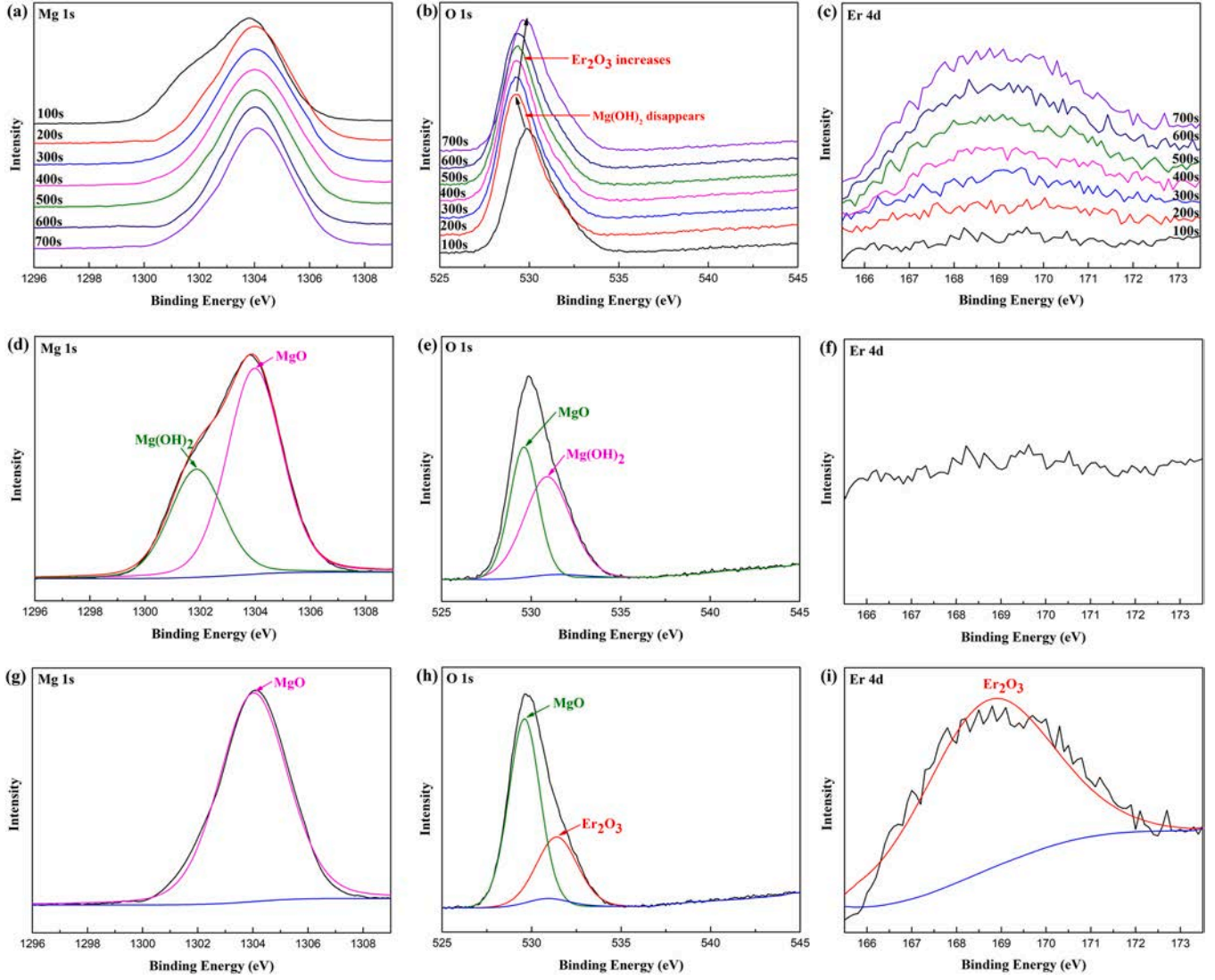
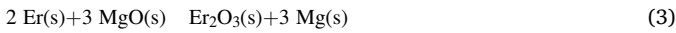
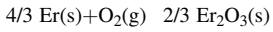


Fig. 11. Depth profiling XPS spectra of the oxide films formed on E1 alloy of (a) Mg 1 s, (b) O 1 s and (c) Er 4d; XPS spectra with sputtering time 100 s of (d) Mg 1 s, (e) O 1 s and (f) Er 4d; and XPS spectra with sputtering time 700 s of (g) Mg 1 s, (h) O 1 s and (i) Er 4d.



The standard Gibbs free energies of reactions (1), (2) and (3) calculated using Factsage software are:

$$\Delta G_1^0(500^\circ\text{C}) = 1205010 + 219.49T - 1035344 [\text{J/mol of O}_2] \quad (4)$$

$$\Delta G_2^0(500^\circ\text{C}) = 1261150 + 189.63T - 1114566 [\text{J/mol of O}_2] \quad (5)$$

Using Eqs. (4) and (5), the standard Gibbs free energy of reaction (3) can be derived as:

$$\Delta G_3^0(500^\circ\text{C}) = 84210 + 44.79T - 118833 [\text{J/mol}] \quad (6)$$

The change in the Gibbs free energy of reaction (1) (2) and (3), ΔG_1 , ΔG_2 and ΔG_3 can be calculated by the following equation:

$$\Delta G_1 = \Delta G_1^0 + RT \ln \frac{a_{\text{MgO}}^2}{a_{\text{Mg}}^2 \cdot p_{\text{O}_2}} [\text{J/mol}] \quad (7)$$

$$\Delta G_2 = \Delta G_2^0 + RT \ln \frac{a_{\text{Er}_2\text{O}_3}^{2/3}}{a_{\text{Er}}^{4/3} \cdot p_{\text{O}_2}} [\text{J/mol}] \quad (8)$$

$$\Delta G_3 = \Delta G_3^0 + RT \ln \frac{a_{\text{Er}_2\text{O}_3} \cdot a_{\text{Mg}}^3}{a_{\text{Er}}^2 \cdot a_{\text{MgO}}^3} [\text{J/mol}] \quad (9)$$

where R is gas constant [J/mol K], T is temperature [K] and a_x is activity. For simplification, the atomic concentrations of Mg and Er are substituted for their elemental activities, and the activities of MgO and Er_2O_3 are expressed as unity. Fig. 13 presents the relationship between the Gibbs free energy change of reaction (1), (2) and (3), ΔG_1 , ΔG_2 , and ΔG_3 , with the atom fraction of Er at 500 °C. As shown in the Fig. 13, ΔG_1 and ΔG_2 are negative for the investigated alloys, indicating the thermodynamic possibility for the occurring of reactions (1) and (2).

The ΔG_3 value can be used to determine the priority of the formation of Er_2O_3 and MgO. When ΔG_3 is negative, Er_2O_3 is preferentially formed on the surface, and when ΔG_3 is positive, MgO is preferentially formed. Therefore, the ΔG_3 value can control the oxidation process of Mg-Er alloys. The Er concentration corresponding to $\Delta G_3 = 0$ is called as the critical concentration of Er, and the critical concentration of Er is 9.66×10^{-3} at% (0.07 wt%) calculated by Eq. (9). When the Er concentration is larger than the critical concentration, ΔG_3 is negative, which indicates that Er_2O_3 is formed prior to MgO. ΔG_3 values

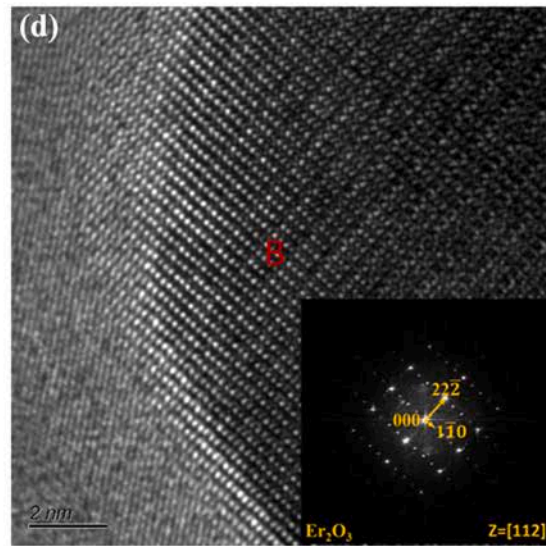
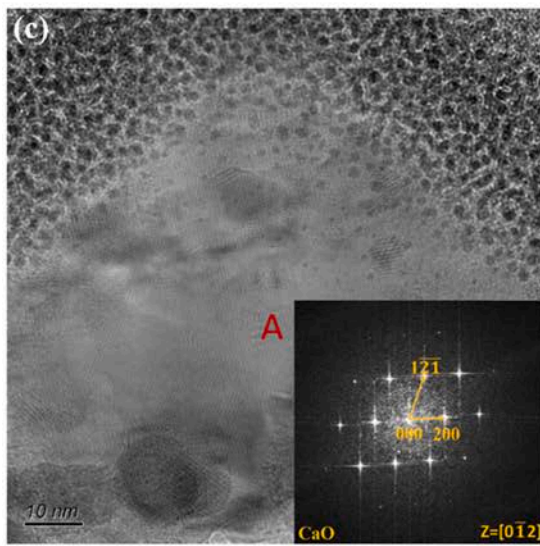
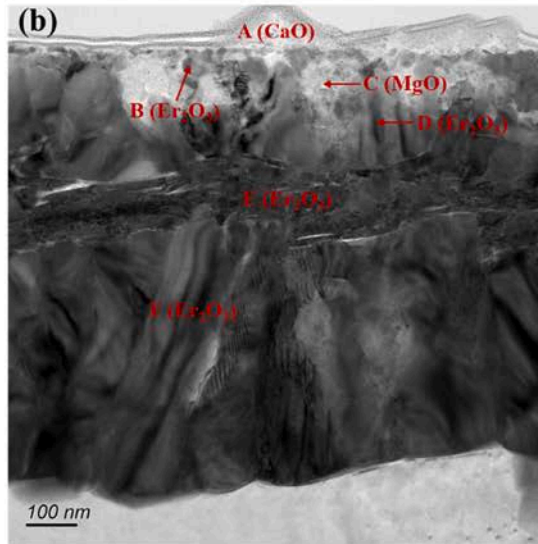
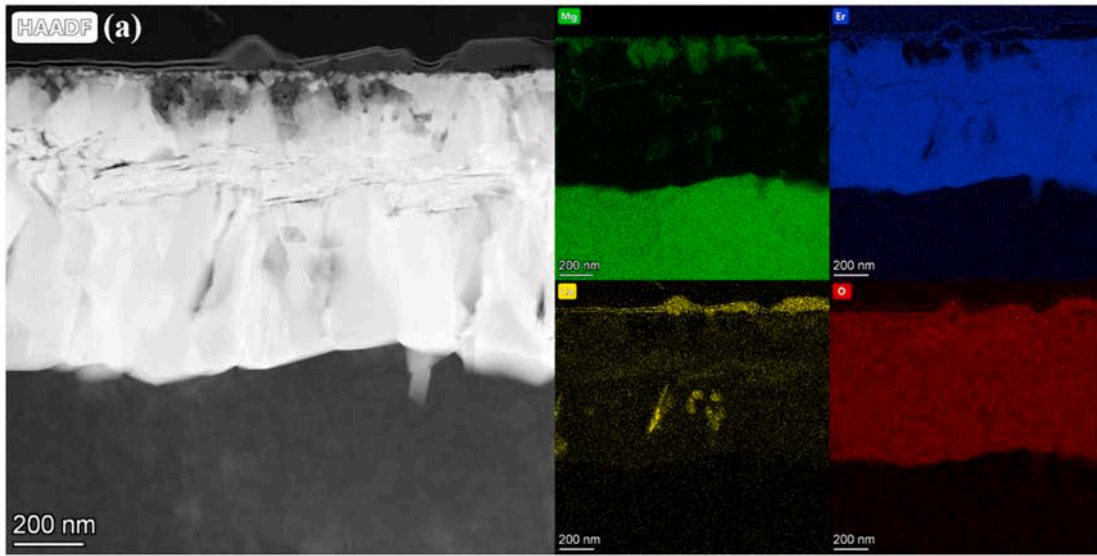


Fig. 12. (a) HAADF-STEM image and the corresponding EDS element maps for Mg, Er, Ca and O elements of the cross-sectional oxide film formed on E4 alloy; (b) bright-field TEM image; (c)-(h) the high-resolution images and digital diffractogram obtained by the fast Fourier transform (FFT) (inserted images) corresponding to different regions in (b).

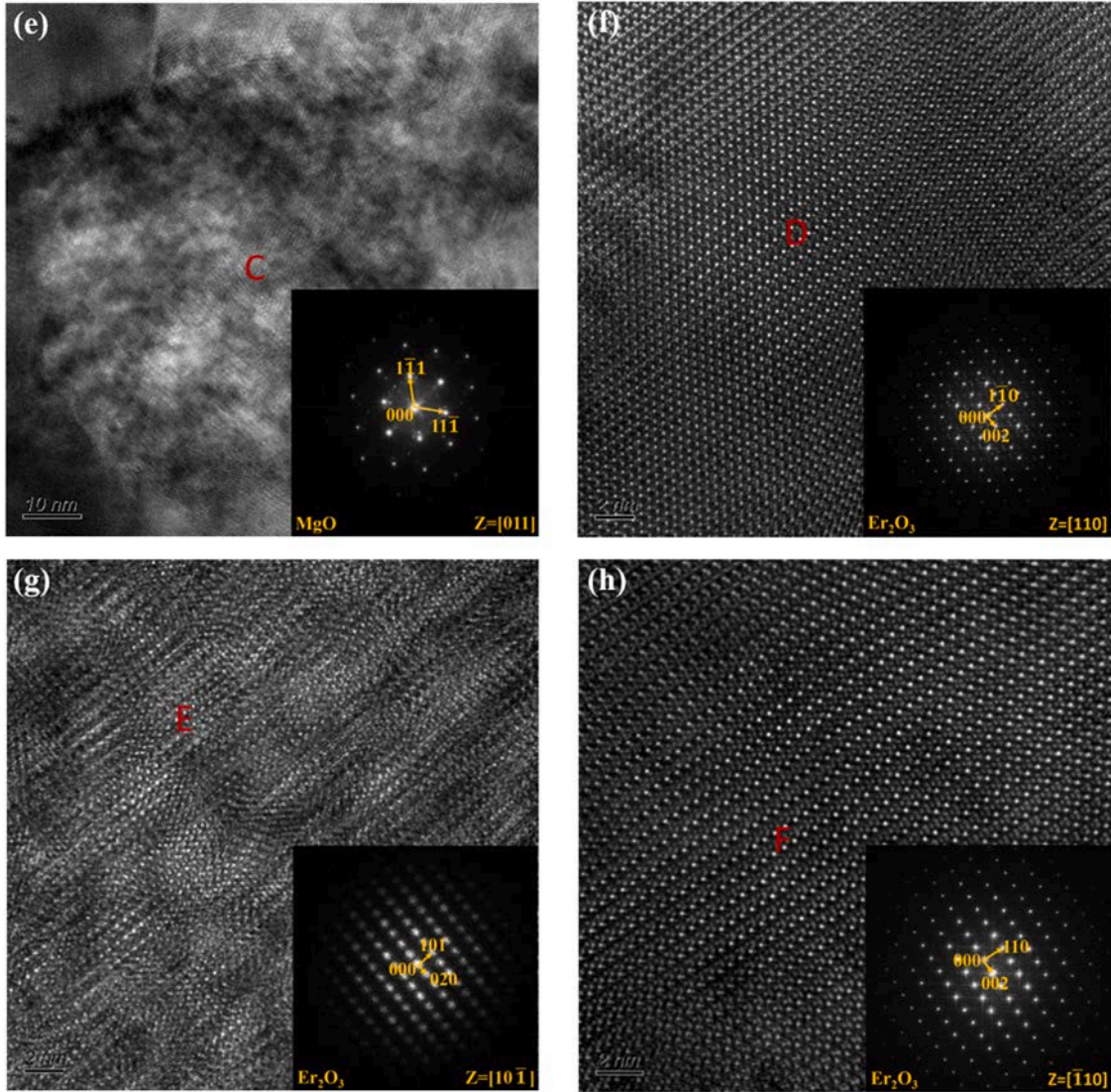


Fig. 12. (continued).

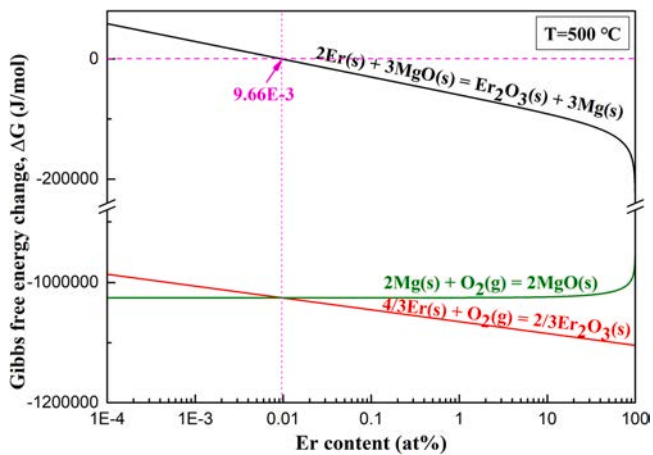


Fig. 13. Relationship between ΔG for the reaction (1), (2) and (3) at 500 °C and atom fraction of Er.

corresponding to the Er content at the oxide/metal interface after oxidation at 500 °C for 100 h are summarized in Table 5. For the E1 alloy, the Er content at the metal/oxide interface is below the critical concentration of Er, indicating the prefer formation of MgO at this interface. However, for the E2, E3 and E4 alloys, the Er contents at the metal/oxide interface are larger than the critical concentration of Er, and Er_2O_3 is preferentially formed at the interface. This is consistent with the results that continuous Er_2O_3 oxide layers on the surface and underneath Er depletion zones in the matrix are observed for the E2, E3 and E4 alloys, and for E1 alloy, intermittently distributed Er_2O_3 on the surface with slight Er depletion zone are observed. Therefore, the Er content at the metal/oxide interface directly controls the priority order of the oxidation reaction, thereby directly affecting the formation of oxidation products.

According to the XPS results in Fig. 11 and TEM results in Fig. 12, MgO tends to form on the outer side of the oxide film of Mg-Er alloys. In the initial stage of oxidation, since ΔG_1 and ΔG_2 are negative, Mg and Er can be oxidized at the same time. The atomic radius of Er is larger than that of Mg, so it can be inferred that the diffusion of Er in Mg should be slower than the self-diffusion of Mg. Thus, MgO can be accumulated more quickly on the outside of the oxide film. As the oxidation proceeding, due to the formation of the oxide film, the oxidation partial pressure in the oxide film decreases and Er_2O_3 with low formation

Table 5

ΔG_3 values corresponding to the Er content at the oxide/metal interface after oxidation at 500 °C for 100 h.

Er contents and ΔG_3	E1	E2	E3	E4
Er content at oxide/metal interface (wt%)	0.03	0.46	1.84	3.51
Er content at oxide/metal interface (at%)	4.31×10^{-3}	6.64×10^{-2}	2.69×10^{-1}	5.20×10^{-1}
Corresponding ΔG_3 (J/mol)	1.04×10^{-4}	-2.48×10^{-4}	-4.28×10^{-4}	-5.13×10^{-4}

pressure can be formed below MgO. In addition, for the E4 alloy, since it contains impurity element Ca, a non-uniform thin CaO layer is formed on the outermost of the oxide film. This is attributed to the much faster diffusion of Ca in Mg than the self-diffusion of Mg [25], leading to the CaO formation in the outermost of the oxide film.

For the E4 alloy, the Er_2O_3 formed on the inner side (area F) of the oxide film is much coarser than the outer side (area E), as shown in Fig. 12. The detailed oxidation process and the formation mechanism of this four-sublayers film is illustrated in Section 4.4.

4.2. The diffusion of erbium

The continuous oxidation of Er on the surface of Mg-Er alloys relies on the diffusion of Er from the matrix to the oxide/metal interface. Thus, the diffusion amount of Er can be related to the amount of Er_2O_3 formed on the surface. During the entire oxidation process at 500 °C for 100 h, the total amount of Er diffused from the matrix to the oxide/metal interface can be approximately interpreted by the content of Er in the diffusion layer deviated from that of in the matrix, which is shown as S1, S2, S3 and S4 in Fig. 10. It can be seen that $S1 < S2 < S3 < S4$. For E2, E3 and E4 alloys, the oxides formed on the surface are mainly composed of Er_2O_3 , indicating that the weight gain during oxidation is mainly derived from the oxidation of Er. As shown in Fig. 4, after oxidation at 500 °C for 100 h, the weight gain of those three alloys follows: $\Delta m_2 < \Delta m_3 < \Delta m_4$, which is consistent with the order of the diffusion amount of Er.

Deriving the fitting functions of the weight gain curves (Fig. 4), the weight gain rate curves can be obtained, as shown in Fig. 14(a). Since the E1 alloy undergoes accelerated oxidation after 45 h, the weight gain rate curve is only plotted for the parabolic oxidation stage within 45 h here. The weight gain rate of the four alloys decreases sharply in the initial stage of oxidation, and then stabilized. Higher Er concentration results in an increasing weight gain rate, i.e. in higher oxidation rates.

For E2, E3, E4, the weight gain mainly corresponds to the mass of oxygen participating in the oxidation reaction of Er, from which the consumption mass of Er during the reaction can be obtained. Therefore, the weight gain rate corresponds to the consumption rate of O (J_{O}), and then the Er consumption rate (J_{Er}) can be obtained. The weight gain rate curves near 100 h were partially enlarged, as shown in Fig. 14(b), and the weight gain rate of the E2, E3 and E4 alloys at 100 h were calculated,

which were 3.11×10^{-4} , 6.71×10^{-4} and $1.32 \times 10^{-3} \text{ mg}\cdot\text{cm}^{-2}\cdot\text{h}^{-1}$, respectively. Thus, the O consumption rates and the Er consumption rates of E2, E3 and E4 can be calculated, as summarized in Table 6. The consumption of Er on the surface comes from the diffusion of Er in the underlying matrix. Therefore, the Er consumption rate equals to the Er flux from the matrix to the surface. Assuming Er diffusion reaches steady state, the Er flux is expressed by Fick's first law:

$$J_{\text{Er}} = D_{\text{Er}} \frac{\partial c_{\text{Er}}}{\partial x} \quad (10)$$

where the Er flux J_{Er} is expressed in $\text{mg}\cdot\text{cm}^{-2}\cdot\text{s}^{-1}$, Er concentration c_{Er} in $\text{mg}\cdot\text{cm}^{-3}$ and x in cm. D_{Er} ($\text{cm}^2\cdot\text{s}^{-1}$) is the inter-diffusion coefficient of Er in the alloy. In order to calculate the value of $\frac{\partial c_{\text{Er}}}{\partial x}$, we transformed the unit of abscissa and ordinate in Fig. 10 to obtain Fig. 15. Accordingly, the values of $\frac{\partial c_{\text{Er}}}{\partial x}$ and D_{Er} can be calculated and are shown in Table 6. Although the obtained values have little differences, the dependence of D on the composition can't be further extracted here since the obtained values are obtained from static equations. So far, there is still no experimental study on the diffusion behavior of the Mg-Er system, and the only corresponding research was reported by Zhong, who used first principles to calculate the diffusion coefficient of Er in Mg [52]. The results of Zhong are shown by line in Fig. 16, and it was compared with the result of our present work. At 500 °C, the Er diffusion coefficient in Mg calculated using first-principles by Zhong [52] is $7.86 \times 10^{-15} \text{ m}^2/\text{s}$, and our present data is $2.70 \sim 4.17 \times 10^{-14} \text{ m}^2/\text{s}$. The results of the two are close to each other, indicating that the data of this experiment can provide a certain reference for the follow-up diffusion research of the Mg-Er system.

4.3. Comparison of oxidation kinetics of Mg-Er alloys with that of the other reactive-element-containing Mg alloys

A variety of Mg alloys with parabolic protective oxidation behavior have been reported in literatures (Mg-Gd alloys [19], Mg-Gd-Y alloys [53], Mg-Gd-Ca alloys [25], Mg-Y alloys [24,29], Mg-Nd alloys [37] and Mg-Nd alloys [40,43]). Fig. 17 summarizes the parabolic oxidation constants (k_p) for Mg alloy oxidation at 500 °C in literature and compares them with the results of the present work. The results show that as the contents of reactive elements increase, the parabolic oxidation

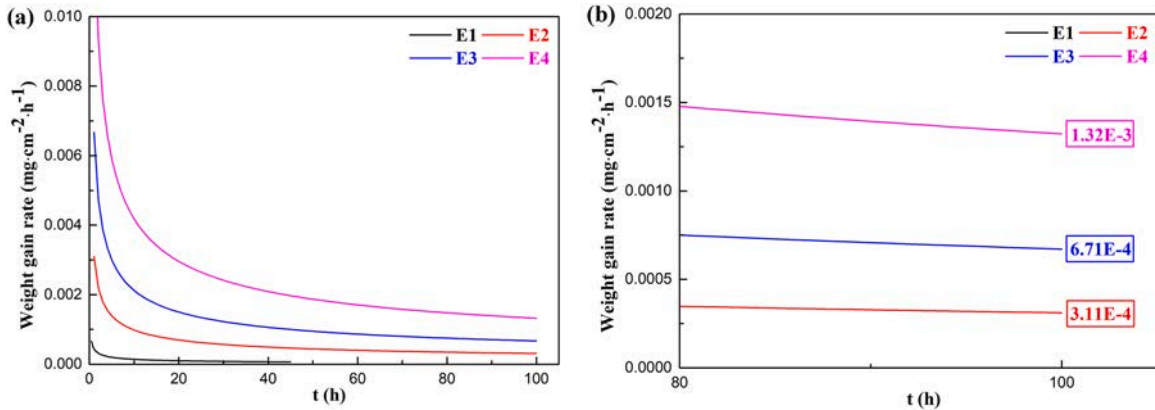


Fig. 14. (a) Weight gain rate ($\text{mg}\cdot\text{cm}^{-2}\cdot\text{h}^{-1}$) curves of Mg-Er alloys during oxidation at 500 °C for 100 h, (b) regional enlarged the weight gain rate curves near 100 h.

Table 6

The summary of O absorption rates, the Er consumption rates and calculated D_{Er} .

Specimens	J_O ($g^2 \cdot cm^{-4} \cdot h^{-1}$)	J_O ($g^2 \cdot cm^{-4} \cdot s^{-1}$)	J_{Er} ($g^2 \cdot cm^{-4} \cdot s^{-1}$)	$\frac{\partial c}{\partial x}$ ($g \cdot cm^{-4}$)	D_{Er} ($m^2 \cdot s^{-1}$)
E2	3.11×10^{-7}	8.64×10^{-11}	6.01×10^{-10}	2.23	2.70×10^{-14}
E3	6.71×10^{-7}	1.86×10^{-10}	1.30×10^{-9}	3.72	3.49×10^{-14}
E4	1.32×10^{-6}	3.67×10^{-10}	2.55×10^{-9}	6.12	4.17×10^{-14}

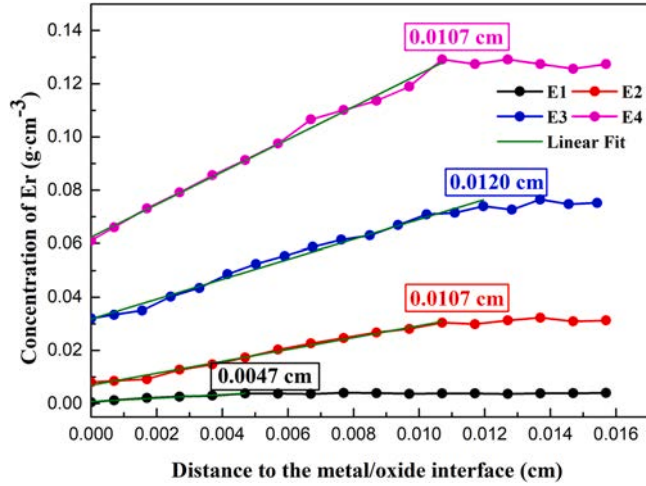


Fig. 15. The concentration of Er with depth subscale detected by EPMA.

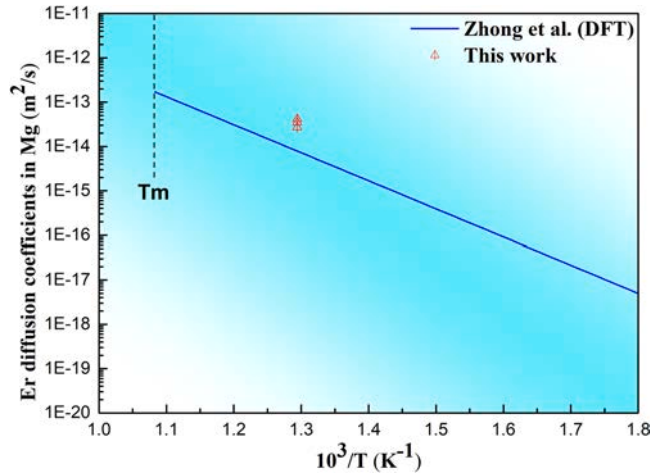


Fig. 16. Er diffusion coefficients in α -Mg by first-principles calculations [52] in comparison with data of this work.

constants generally show an increasing trend, which is consistent with the results of the present work. The k_p values of the Mg-Er alloy in the present work are at a low level in the range of Er content of 0.5–8.1 wt%, which is lower than that of other alloys. Therefore, the Er element seems to be an ideal element to improve the high-temperature oxidation resistance of magnesium alloys. It is worth noting that the k_p value of E1 alloy corresponds to the initial protective oxidation stage ($0 < t < 45$ h), and with the time increasing, the E1 alloy undergoes accelerated oxidation. The lower oxidation rate in the limited time for E1 alloy comparable with that of other E2, E3, E4 alloys is because that for E1 alloy, the formed oxides is mixture of MgO and Er_2O_3 and the accumulated oxygen fraction for MgO is lower than that of Er_2O_3 . Therefore, from the perspective of long-term oxidation, the oxidation resistance of E1 alloy is inferior to that of higher Er containing alloys, here these are, E2, E3 and E4 alloys.

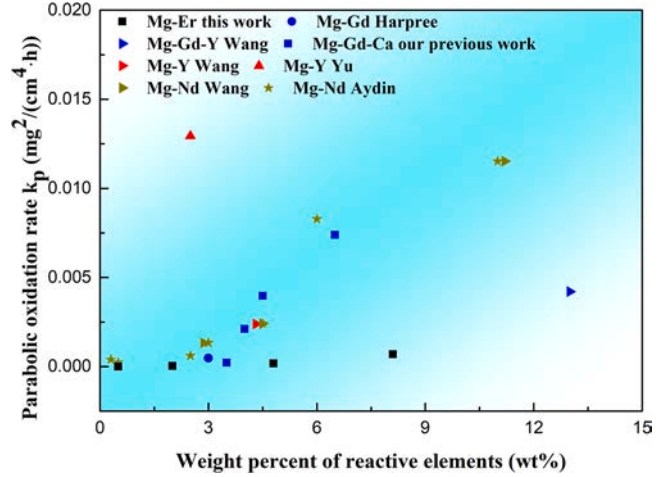


Fig. 17. The summary of parabolic rate constants (k_p) of Mg alloys oxidation at 500 °C in literature and present work.

The enhancement of the high-temperature oxidation resistance of Mg by alloying with rare elements (REs) is mainly attributed to the formation of compact RE oxide film on the surface [19,31,40,41,54,55]. In the RE oxides, the metal substructure is rigid below its melting temperatures. It is reported for RE oxides, its growth is mainly dominated by the inward diffusion of oxygen anions [56]. In lanthanide oxides, oxygen anion transport rates rapidly decrease with increasing atomic number of the lanthanide metal [43]. Thus, the oxygen mobility in Nd_2O_3 is higher than that of Gd_2O_3 and Er_2O_3 . As shown in Fig. 16, the k_p values of Mg-Nd alloys are much higher than that of Gd or Er-containing Mg alloys, which can be explained by the fast-inward diffusion of oxygen anion in oxide film. The diffusion of oxygen anions in single crystals of Y_2O_3 and Er_2O_3 was investigated by a thermobalance technique by Berard et al. [43], and D_0 and E_a values for Y_2O_3 and Er_2O_3 are $6.06 \times 10^{-6} \text{ cm}^2/\text{s}$, $1.6 \times 10^5 \text{ cal/mol}$, and $1.31 \times 10^{-4} \text{ cm}^2/\text{s}$, $3.0 \times 10^3 \text{ cal/mol}$, respectively [57]. Thus, the diffusion coefficient of oxygen anions in single crystal of Y_2O_3 and Er_2O_3 at 500 °C can be calculated to be $1.75 \times 10^{-15} \text{ m}^2/\text{s}$ and $3.95 \times 10^{-17} \text{ m}^2/\text{s}$. The much faster diffusion of oxygen anions in Y_2O_3 can result in a larger k_p compared with that of Er_2O_3 . For alloys containing Nd or Y, internal oxidation can be observed due to the faster diffusion of oxygen anions in their corresponding RE oxides [31,41,43,49,58,59].

4.4. The oxidation stages of the Mg-Er alloy

According to the composition of the oxide layers and the distribution of the elements, a scheme of the oxidation process is proposed for the studied alloys. In the initial stage of oxidation, the outmost layer of Mg and Er are simultaneously oxidized to form MgO and Er_2O_3 which are thermodynamic possible. In the second stage, as the oxidation progresses, the Er at the surface is continuously consumed. In order to maintain the oxidation of the Er on the surface, the Er in matrix diffuse to the metal/oxide interface, and a diffusion layer of Er is formed sub-scale. When the Er content at the interface is less than the critical concentration of Er, MgO is preferentially formed at the interface, such as the E1 alloy. When a large amount of Mg is oxidized in the local area,

oxide nodules can be formed (as shown in Fig. 6), which triggers subsequent accelerated oxidation.

For the E2, E3 and E4 alloys, the Er concentration at the oxide/metal interface is larger than the critical concentration of Er, Er_2O_3 is preferentially formed at the interface, which is promoting the formation of a continuous Er_2O_3 layer. Once the continuous Er_2O_3 layer is formed, subsequent oxidation occurs only by the Er_2O_3 layer thickening and Mg is no longer oxidized [59,60].

In order to understand how the continuous Er_2O_3 film improves the oxidation resistance of Mg-Er alloys, taking E4 alloy as an example, a hypothesis for the evolution of the oxide film of this alloy is schematically depicted in Fig. 18. The four-stage oxidation process is described as follows:

(1) In the first stage of oxidation, as shown in Fig. 18(a), the high reactive impurity, here the 323 ppm Ca, in the alloy, enriches on the surface and is oxidized to form CaO. This layer is quite thin, here with an average thickness of ~ 20 nm, and not uniform. Such an extremely thin and uneven CaO film cannot effectively hinder the inward diffusion of oxygen.

(2) In the second stage of oxidation, as shown in Fig. 18(b), when the alloy exposed in air, the outer layer of Mg and Er instantly react with oxygen to form a composite oxides layer composed of MgO and Er_2O_3 . The thickness of this composite layer is about 150 nm. This composite layer is not compact and still cannot effectively hinder the inward diffusion of oxygen.

(3) In the third stage of oxidation, since the composite oxide layer is

not compact, the oxygen can still freely diffuse into the substrate and a layer of pure Er_2O_3 is formed. This oxide formation is still reaction-controlled. As a result, a fine and continuous Er_2O_3 layer with a thickness of about 100 nm is formed, as shown in Fig. 18(c), which can effectively prohibit the inward diffusion of oxygen, thereby significantly reducing subsequent oxygen diffusion.

(4) In the fourth stage of oxidation, the oxygen diffused from the third stage formed compact layer is comparatively slower. Therefore, the oxidation of Er at this stage tends to continue via the growing on the crystal grains formed in the third stage and the formation is diffusion-controlled, resulting in a columnar and coarse Er_2O_3 oxide layer which follows the parabolic growth behavior, as shown in Fig. 18(d).

The first three stages are considered to be a short transient period where the involved reactions are reaction-controlled and fast. A compact Er_2O_3 layer was formed in the third stage resulting in the followed parabolic growth of the fourth layer. For the weight-gain curve of the E4 alloy, the transient stage before the oxidation process following parabolic kinetics is too short to be identified. Hence, for the long-term oxidation process, the oxidation kinetics were mainly controlled by diffusion.

5. Conclusion

The long-term oxidation behavior of Mg-Er binary alloys at 500 °C was studied using semi in-situ oxidation experiments by measuring the weight gain during the oxidation procedure. The oxidation processes

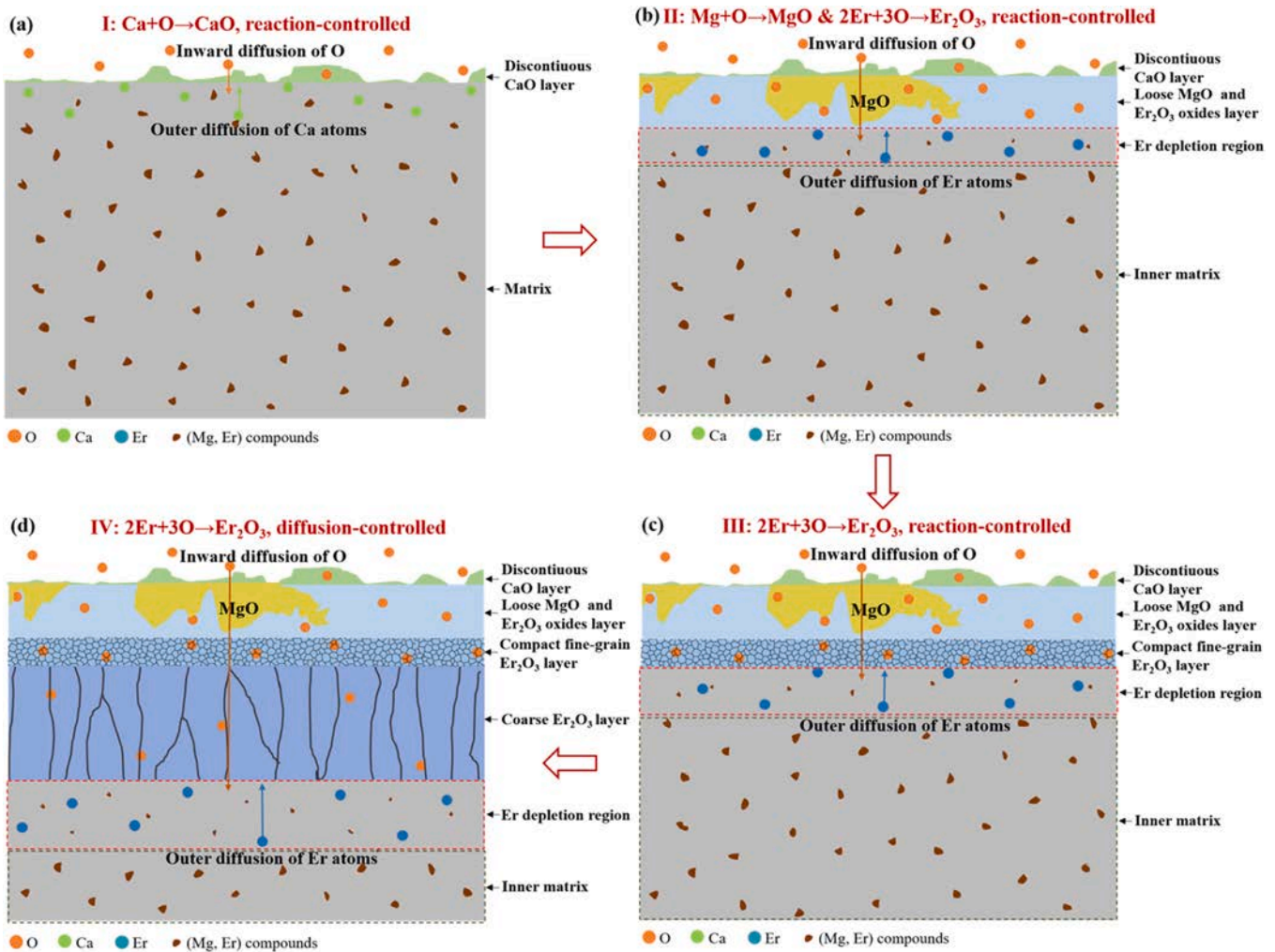


Fig. 18. Schematic diagrams of multi-layered oxide film structures formed on the E4 alloys at 500 °C in air.

were analyzed with respect of thermodynamics, kinetics and oxides-film formation process. The following conclusions can be drawn:

- (1) The oxidation of Mg-0.5 wt% Er alloy undergoes a transformation of oxidation kinetics, with the parabolic law of protective oxidation transforming into the power law of accelerated oxidation at 500 °C after 45 h. When the content of Er is larger than 1.9 wt%, the alloys exhibit protective oxidation during the studied oxidation process (500 °C for 100 h).
- (2) The oxidation resistance of Mg-Er alloy is closely related to the continuity of the Er₂O₃ layer. A continuous Er₂O₃ layer was formed on the alloys with Er content larger than 1.9 wt%, subsequent oxidation occurs only by the Er₂O₃ layer thickening and Mg is no longer oxidized. On the contrary, a discontinuous Er₂O₃ layer was formed on Mg-0.5 wt% Er alloy, which cannot prevent the subsequent formation of MgO, resulting in catastrophic oxidation.
- (3) The continuity of the Er₂O₃ is related to Er concentration at the metal/oxide interface. For the E1 alloy, the Er concentration at the metal/oxide interface is less than its critical concentration, leading to a preferential formation of MgO at the interface. The situation is the opposite for the alloys with Er content larger than 1.9 wt%.
- (4) The continuous oxidation of Er on the surface of Mg-Er alloys relies on the diffusion of Er from the matrix to the oxide/metal interface, which causes a depletion of Er layer under the oxide film.
- (5) The surface film of Mg-8.1Er (wt%) alloy was composed of four sublayers. Beneath an instantly formed high-reactivity trace-impurity oxide layer and a thin MgO and Er₂O₃ mixture layer, the double Er₂O₃ layers consisting of a compact fine-grain layer and an underlying coarse-columnar-grain layer providing the protective effect. A four-stage oxidation process composed of three transient reaction-controlled oxidation processes and followed by a diffusion-controlled oxide growth process is proposed.

Declaration of Competing Interest

The authors declare that they have no known competing financial interests or personal relationships that could have appeared to influence the work reported in this paper.

Data availability

The raw/processed data required to reproduce these findings are available on request.

Acknowledgments

This work is financially supported by National Natural Science Foundation of China (51971044, U1910213 and 52171100) and the Natural Science Foundation of Chongqing (cstc2019yszx-jcyjX0004). The authors also thank the 111 project (B16007, fund by the Ministry of Education of the People's Republic of China) and the technology support by Karlsruhe Nano Micro Facility (KNMF), KIT.

References

- [1] F. Czerwinski, The reactive element effect on high-temperature oxidation of magnesium, *Int. Mater. Rev.* 60 (2015) 264–296.
- [2] J. Song, J. She, D. Chen, F. Pan, Latest research advances on magnesium and magnesium alloys worldwide, *J. Magnes. Alloy* 8 (2020) 1–41.
- [3] C.L. Cheng, Q. Lan, Q.Y. Liao, Q.C. Le, X.Q. Li, X.R. Chen, J.Z. Cui, Effect of Ca and Gd combined addition on ignition temperature and oxidation resistance of AZ80, *Corros. Sci.* 160 (2019), 108176.
- [4] T. Chen, Y. Yuan, J. Wu, T. Liu, F. Pan, Alloy design strategies of the native anti-corrosion magnesium alloy, in: V. Joshi (Ed.), *Magnes. Technol.* 2019, *Miner., Met. Mater. Ser.* 2019 (2019) 169–173.
- [5] J. Wang, Y. Yuan, X. Cheng, T. Chen, F. Pan, The high-solution design of magnesium alloys (invited speak), in: V.M. Mille (Ed.), *TMS 2021, Magnesium Technology 2021, The Minerals, Metals & Materials Series*, USA, 2021, https://doi.org/10.1007/978-3-030-65528-0_5.
- [6] C. Zhang, L. Wu, H. Liu, G.S. Huang, B. Jiang, A. Atrens, F.S. Pan, Microstructure and corrosion behavior of Mg-Sc binary alloys in 3.5 wt% NaCl solution, *Corros. Sci.* 174 (2020), 108831.
- [7] T. Chen, Y. Yuan, T.T. Liu, D.J. Li, A.T. Tang, X.H. Chen, R. Schmid-Fetzer, F. S. Pan, Effect of Mn addition on melt purification and Fe tolerance in Mg alloys, *Jom* 73 (2021) 892–902.
- [8] T. Chen, Q. Gao, Y. Yuan, T. Li, Q. Xi, T. Liu, A. Tang, A. Watson, F. Pan, Coupling physics in machine learning to investigate the solution behavior of binary Mg alloys, *J. Magnes. Alloy* (2021), <https://doi.org/10.1016/j.jma.2021.06.014>.
- [9] G. Wu, C. Wang, M. Sun, W. Ding, Recent developments and applications on high-performance cast magnesium rare-earth alloys, *J. Magnes. Alloy* 9 (2020) 1–20.
- [10] J. Xie, J. Zhang, Z. You, S. Liu, J. Feng, Towards developing Mg alloys with simultaneously improved strength and corrosion resistance via RE alloying, *J. Magnes. Alloy* 9 (2020) 41–56.
- [11] F. Cao, B. Xiao, Z. Wang, T. Ying, D. Zheng, A. Atrens, G.L. Song, A Mg alloy with no hydrogen evolution during dissolution, *J. Magnes. Alloy* (2021), <https://doi.org/10.1016/j.jma.2021.08.024>.
- [12] F. Czerwinski, The oxidation behaviour of an AZ91D magnesium alloy at high temperatures, *Acta Mater.* 50 (2002) 2639–2654.
- [13] F. Czerwinski, Overcoming barriers of magnesium ignition and flammability, *Adv. Mater. Process* 172 (2014) 28–31.
- [14] F. Czerwinski, Factors affecting the oxidation nature of magnesium alloys, *JOM-US* 56 (2004) 29–31.
- [15] F. Czerwinski, Oxidation characteristics of magnesium alloys, *JOM-US* 64 (2012) 1477–1483.
- [16] F. Czerwinski, Controlling the ignition and flammability of magnesium for aerospace applications, *Corros. Sci.* 86 (2014) 1–16.
- [17] V. Fournier, P. Marcus, I. Olefjord, Oxidation of magnesium, *Surf. Interface Anal.* 34 (2002) 494–497.
- [18] J. Medved, P. Mrvar, M. Voncina, Oxidation resistance of cast magnesium alloys, *Oxid. Met* 71 (2009) 257–270.
- [19] H.S. Brar, I.S. Berglund, J.B. Allen, M.V. Manuel, The role of surface oxidation on the degradation behavior of biodegradable Mg-RE (Gd, Y, Sc) alloys for resorbable implants, *Mat. Sci. Eng. C -Mater.* 40 (2014) 407–417.
- [20] D.B. Lee, High temperature oxidation of AZ31+0.3 wt%Ca and AZ31+0.3 wt%CaO magnesium alloys, *Corros. Sci.* 70 (2013) 243–251.
- [21] J.K. Lee, S.K. Kim, Effect of CaO composition on oxidation and burning behaviors of AM50 Mg alloy, *Trans. Nonferr. Met. Soc.* 21 (2011) 23–27.
- [22] Q.Y. Tan, N. Mo, B. Jiang, F.S. Pan, A. Atrens, M.X. Zhang, Oxidation resistance of Mg-9Al-1Zn alloys micro-alloyed with Be, *Scr. Mater.* 115 (2016) 38–41.
- [23] X.M. Wang, X.Q. Zeng, G.S. Wu, S.S. Yao, Y.J. Lai, Surface analysis and oxidation behavior of Y-ion implanted AZ31 magnesium alloys, *Appl. Surf. Sci.* 253 (2007) 3574–3580.
- [24] X.M. Wang, X.Q. Zeng, Y. Zhou, G.S. Wu, S.S. Yao, Y.J. Lai, Early oxidation behaviors of Mg-Y alloys at high temperatures, *J. Alloy Compd.* 460 (2008) 368–374.
- [25] J.J. Wu, Y. Yuan, X.W. Yu, T. Chen, D.J. Li, L. Wu, B. Jiang, A. Atrens, F.S. Pan, The high-temperature oxidation resistance properties of magnesium alloys alloyed with Gd and Ca, *J. Mater. Sci.* 56 (2021) 8745–8761.
- [26] B.S. You, W.W. Park, I.S. Chung, The effect of calcium additions on the oxidation behavior in magnesium alloys, *Scr. Mater.* 42 (2000) 1089–1094.
- [27] X.Q. Zeng, Q.D. Wang, Y.H. Lu, W.J. Ding, Y.P. Zhu, C.Q. Zhai, C. Lu, X.P. Xu, Behavior of surface oxidation on molten Mg-9Al-0.5Zn-0.3Be alloy, *Mat. Sci. Eng. A-Struct.* 301 (2001) 154–161.
- [28] Q.Y. Tan, N. Mo, C.L. Lin, B. Jiang, F.S. Pan, H. Huang, A. Atrens, M.X. Zhang, Improved oxidation resistance of Mg-9Al-1Zn alloy microalloyed with 60 wt ppm Be attributed to the formation of a more protective (Mg,Be)O surface oxide, *Corros. Sci.* 132 (2018) 272–283.
- [29] X.W. Yu, B. Jiang, J.J. He, B. Liu, F.S. Pan, Oxidation resistance of Mg-Y alloys at elevated temperatures and the protection performance of the oxide films, *J. Alloy Compd.* 749 (2018) 1054–1062.
- [30] X.W. Yu, B. Jiang, H. Yang, Q.S. Yang, X.S. Xia, F.S. Pan, High temperature oxidation behavior of Mg-Y-Sn, Mg-Y, Mg-Sn alloys and its effect on corrosion property, *Appl. Surf. Sci.* 353 (2015) 1013–1022.
- [31] S. Inoue, M. Yamasaki, Y. Kawamura, Classification of high-temperature oxidation behavior of Mg-1 at% X binary alloys and application of proposed taxonomy to nonflammable multicomponent Mg alloys, *Corros. Sci.* 174 (2020), 108858.
- [32] X.W. Yu, B. Jiang, J.J. He, B. Liu, Z. Jiang, F.S. Pan, Effect of Zn addition on the oxidation property of Mg-Y alloy at high temperatures, *J. Alloy Compd.* 687 (2016) 252–262.
- [33] M.D. López, C.J. Múñez, M. Carboneras, P. Rodrigo, M.D. Escalera, E. Otero, Influence of temperature on oxidation behaviour of ZE41 magnesium alloy, *J. Alloy Compd.* 491 (2010) 131–136.
- [34] Q.Y. Tan, N. Mo, B. Jiang, F.S. Pan, A. Atrens, M.X. Zhang, Combined influence of Be and Ca on improving the high-temperature oxidation resistance of the magnesium alloy Mg-9Al-1Zn, *Corros. Sci.* 122 (2017) 1–11.
- [35] Q.Y. Tan, N. Mo, C.L. Lin, Y.T. Zhao, Y. Yin, B. Jiang, F.S. Pan, A. Atrens, H. Huang, M.X. Zhang, Generalisation of the oxide reinforcement model for the high oxidation resistance of some Mg alloys micro-alloyed with Be, *Corros. Sci.* 147 (2019) 357–371.
- [36] Q.Y. Tan, Y. Yin, N. Mo, M.X. Zhang, A. Atrens, Recent understanding of the oxidation and burning of magnesium alloys, *Surf. Innov.* 7 (2019) 71–92.

- [37] X.M. Wang, X.Q. Zeng, G.S. Wu, S.S. Yao, L.B. Li, Surface oxidation behavior of MgNd alloys, *Appl. Surf. Sci.* 253 (2007) 9017–9023.
- [38] F. Czerwinski, The early stage oxidation and evaporation of Mg-9%Al-1%Zn alloy, *Corros. Sci.* 46 (2004) 377–386.
- [39] Q.Y. Tan, A. Atrens, N. Mo, M.X. Zhang, Oxidation of magnesium alloys at elevated temperatures in air: A review, *Corros. Sci.* 112 (2016) 734–759.
- [40] D.S. Aydin, Z. Bayindir, M. Hoseini, M.O. Pekguleryuz, The high temperature oxidation and ignition behavior of Mg-Nd alloys part I: The oxidation of dilute alloys, *J. Alloy Compd.* 569 (2013) 35–44.
- [41] D.S. Aydin, Z. Bayindir, M.O. Pekguleryuz, The high temperature oxidation behavior of Mg-Nd alloys. Part II: The effect of the two-phase microstructure on the on-set of oxidation and on oxide morphology, *J. Alloy Compd.* 584 (2014) 558–565.
- [42] D.S. Aydin, Z. Bayindir, M.O. Pekguleryuz, High temperature oxidation behavior of hypoeutectic Mg-Sr binary alloys: the role of the two-phase microstructure and the surface activity of Sr, *Adv. Eng. Mater.* 17 (2015) 697–708.
- [43] D.S. Aydin, M. Hoseini, M.O. Pekguleryuz, Understanding the high temperature oxidation and ignition behaviour of two-phase Mg-Nd alloys and a comparison to single phase Mg-Nd, *Philos. Mag.* 95 (2015) 259–274.
- [44] H. Seyama, M. Soma, X-ray photoelectron spectroscopic study of montmorillonite containing exchangeable divalent-cations, *J. Chem. Soc. Farad T* 1 80 (1984) 237–248.
- [45] D.E. Haycock, M. Kasrai, C.J. Nicholls, D.S. Urch, The electronic structure of magnesium hydroxide (brucite) using X-ray emission, X-ray photoelectron, and auger spectroscopy, *J. Chem. Soc. Dalton* 10 (1978), <https://doi.org/10.1002/chin.197908011>.
- [46] R.P. Vasquez, MgO(100) by XPS, *Surf. Sci. Spectra* 2 (1993) 13–19.
- [47] B.D. Padalia, W.C. Lang, P.R. Norris, L.M. Watson, D.J. Fabian, X-ray photoelectron core-level studies of the heavy rare-earth metals and their oxides, *Proc. R. Soc. Lond. A. Math. Phys. Sci.* 354 (1997) 269–290.
- [48] C.D. Wagner, L.E. Davis, J.F. Moulder, G.E. Muilenberg, *Handbook of X-Ray Photoelectron Spectroscopy*, Physical Electronic Division, (1979).
- [49] S. Inoue, M. Yamasaki, Y. Kawamura, Oxidation behavior and incombustibility of molten Mg-Zn-Y alloys with Ca and Be addition, *Corros. Sci.* 149 (2019) 133–143.
- [50] S.M. Lakiza, L.M. Lopato, Phase diagram of the Al₂O₃-ZrO₂-Er₂O₃ system, *J. Eur. Ceram. Soc.* 28 (2008) 2389–2397.
- [51] S.T. Lopato, The phase diagram of the system Y₂O₃-MgO, *Powder Met. Met. Ceram.* 2 (1963) 454–457.
- [52] W. Zhong, J.C. Zhao, A comprehensive diffusion mobility database comprising 23 elements for magnesium alloys, *Acta Mater.* 201 (2020) 191–208.
- [53] W. Xuemin, W. Weidong, T. Yongjian, Z. Xiaoqin, Y. Shoushan, Early high temperature oxidation behaviors of Mg-10Gd-3Y alloys, *J. Alloy Compd.* 474 (2009) 499–504.
- [54] Z.L. Ning, W.Z. Liang, F.Y. Cao, J.F. Sun, The effect of Y on the oxidation of Mg-Zn-Zr Alloys, *Int J. Mod. Phys. B* 23 (2009) 796–801.
- [55] L.Y. Wu, H.T. Li, Effect of selective oxidation on corrosion behavior of Mg-Gd-Y-Zn-Zr alloy, *Corros. Sci.* 142 (2018) 238–248.
- [56] G. Adachi, N. Imanaka, The binary rare earth oxides, *Chem. Rev.* 98 (1998) 1479–1514.
- [57] M.F. Berard, C.D. Wirkus, D.R. Wilder, Diffusion of oxygen in selected monocrystalline rare earth oxides, *J. Am. Ceram. Soc.* 51 (1968) 643–647.
- [58] J.F. Fan, C.L. Yang, G. Han, S. Fang, W.D. Yang, B.S. Xu, Oxidation behavior of ignition-proof magnesium alloys with rare earth addition, *J. Alloy Compd.* 509 (2011) 2137–2142.
- [59] J.F. Fan, G.C. Yang, Y.H. Zhou, Y.H. Wei, B.S. Xu, Selective oxidation and the third-element effect on the oxidation of Mg-Y alloys at high temperatures, *Met. Mater. Trans. A* 40 (2009) 2184–2189.
- [60] J.F. Fan, G.C. Yang, S.L. Cheng, H. Xie, W.X. Hao, M. Wang, Y.H. Zhou, Surface oxidation behavior of Mg-Y-Ce alloys at high temperature, *Met. Mater. Trans. A* 36 (2005) 235–239.